Ocean Engineering 263 (2022) 112364

Contents lists available at ScienceDirect

Ocean Engineering

journal homepage: www.elsevier.com/locate/oceaneng

A systematic investigation on the manoeuvring performance of a ship performing low-speed manoeuvres in adverse weather conditions using CFD

Daejeong Kim [a,*], Jeongbin Yim [b], Soonseok Song [c], Yigit Kemal Demirel [a], Tahsin Tezdogan [a]

[a] Department of Naval Architecture, Ocean and Marine Engineering, University of Strathclyde, 100 Montrose Street, Glasgow, G4 0LZ, UK
[b] Department of Maritime AI and Cyber Security, Korea Maritime & Ocean University, 727, Taejong-ro, Yeongdo-gu, Busan, South Korea
[c] Department of Naval Architecture & Ocean Engineering, College of Engineering, Inha University, 100 Inha-ro, Incheon, South Korea

ARTICLE INFO

Keywords:
Computational fluid dynamics
RANS solver
Ship manoeuvrability
Minimum propulsion power
Adverse weather conditions

ABSTRACT

The International Maritime Organisation (IMO) requirements for the control of greenhouse gas (GHG) emissions of shipping have raised interest in ship manoeuvrability in adverse weather conditions when compliance is accomplished simply by reducing the main engine power. In response, the IMO has adopted the guidelines for determining minimum propulsion power to maintain the manoeuvrability of ships in adverse conditions. In the present paper, a systematic investigation on the manoeuvrability of a ship with different low advance speeds in adverse weather conditions was conducted by means of an unsteady Reynolds-Averaged Navier-Stokes solver. The numerical results demonstrated the contribution of low advance speeds to the course-keeping and turning circle manoeuvre, providing a practical insight into the manoeuvring performance of a ship with minimum propulsion power in adverse weather conditions. For the course-keeping control, the ship experienced more aggressive steering as the propeller revolution decreased in the oblique waves, while it appeared that the difference in the rudder deflection according to the change in the propeller speed in the head, beam, and following waves is negligible. The difficulty of the low speed turning manoeuvre was clearly noted when the direction of the incident wave was opposite to the direction towards which the ship intended to turn. It is believed that this paper can also be impactful in improving the guidelines of minimum powering of ships for safe navigation in adverse weather conditions.

1. Introduction

The introduction of the Energy Efficiency Design Index (EEDI) by the International Maritime Organisation (IMO), aiming to increase energy efficiency and reduce greenhouse gas (GHG) emissions of shipping, has raised interest in ship manoeuvrability in adverse sea states (IMO, 2011). To achieve the stringent requirements of the EEDI regulation, operating ships should reduce carbon dioxide (CO_2) emissions. One way of complying with these demanding EEDI requirements is to reduce the installed main engine power, by which CO_2 emissions and fuel consumption can be decreased. However, vessels with insufficient propulsion power may have poor course-keeping and manoeuvring capabilities especially in rough seas, which can cause a serious ship safety problem (Kim et al., 2022a). In response, the Marine Environment Protection Committee (MEPC) has adopted the guidelines for determining minimum propulsion power to maintain the manoeuvrability of ships in adverse conditions (IMO, 2021). The guidelines put forward by the MEPC state that a vessel with minimum propulsion power should be able to move forward with the speed of 2.0 knots (i.e., the minimum required advance speed) through water in wind and wave directions from head to 30 degrees off-bow when operating in adverse weather conditions. Given this, it is strongly required to evaluate the manoeuvring performance of a ship with low advance speeds in adverse weather conditions such as course-keeping and turning capabilities. The main aim of this study is to provide practical insights into the manoeuvrability of a ship performing low-speed manoeuvres in adverse weather conditions in a broader sense, performing a systematic investigation on the subject.

Within the European funded Project SHOPERA, the experimental investigation was focused on the manoeuvrability of the KVLCC2 and DTC ship models in regular and irregular waves (Papanikolaou et al.,

---

[*] Corresponding author.
E-mail address: daejeong.kim@strath.ac.uk (D. Kim).

https://doi.org/10.1016/j.oceaneng.2022.112364
Received 7 April 2022; Received in revised form 7 August 2022; Accepted 19 August 2022

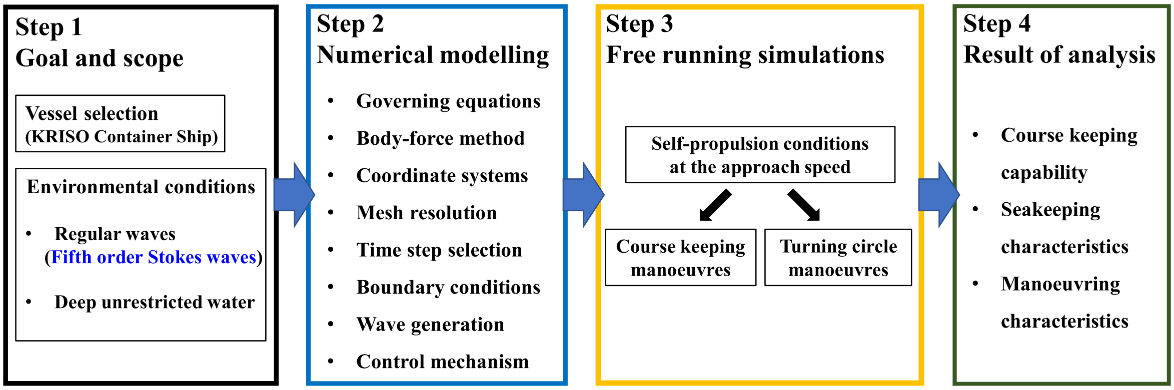

Fig. 1. Research methodology for the free-running CFD simulations.

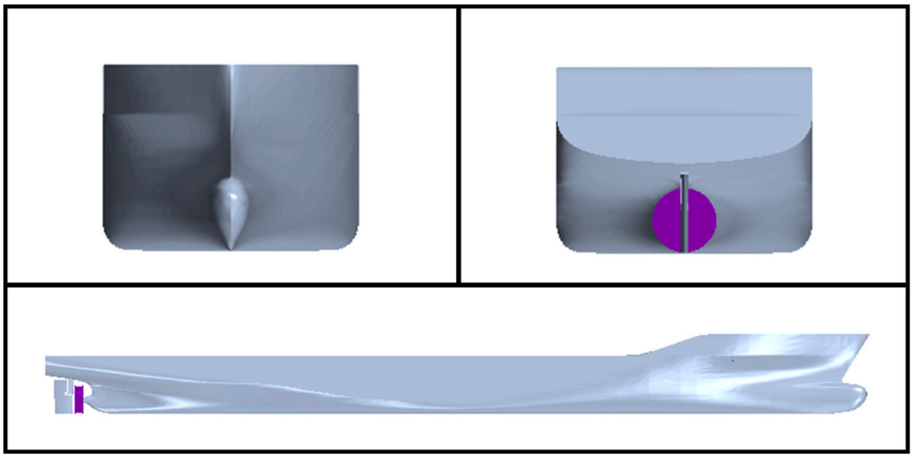

Fig. 2. KCS geometry with a semi balanced rudder and an actuator disk.

Table 1
The principal characteristics of the KCS model used in this study.

Main particulars	Symbols	Model scale (1:75.24)	Full scale
Length between the perpendiculars	L_{BP} (m)	3.057	230.0
Length of waterline	L_{WL} (m)	3.0901	232.5
Beam at waterline	B_{WL} (m)	0.4280	32.2
Draft	D (m)	0.1435	10.8
Displacement	Δ (m^3)	0.1222	52030
Block coefficient	C_B	0.651	0.651
Ship wetted area without rudder	S (m^2)	1.6834	9530
Longitudinal centre of buoyancy	% L_{BP}, fwd+	−1.48	−1.48
Metacentric height	GM (m)	0.008	0.6
Radius of gyration	K_{xx}/B	0.49	0.49
Radius of gyration	K_{yy}/L_{BP}, K_{zz}/L_{BP}	0.25	0.25
Propeller diameter	D_P (m)	0.105	7.9
Propeller rotation direction (view from stern)		Right hand side	Right hand side
Rudder turn rate	(deg/s)	20.1	2.32

2015; el Moctar et al., 2016; Papanikolaou et al., 2016; Sprenger et al., 2016). In their experiments, 6 knots as the minimum required advance speed was selected instead of 2 knots as proposed in IMO (2021), with an aim to consider possibly strong currents in coastal areas. A good discussion of the course-keeping and turning capabilities of a ship with minimum propulsion power in adverse weather conditions is also described in Kim et al. (2022d), who performed extensive free-running model experiments for the tanker KVLCC2. In their research, course-keeping and turning manoeuvres were carried out in long-crested irregular head waves representing sea states 5 and 6, with three kinds of model propulsion points corresponding to the full-scale calm water speeds of 4.0, 7.0, and 15.5 knots. The results demonstrated that the ship's heading control was extremely challenging in port beam and stern quartering waves at sea state 6 when dealing with low-speed manoeuvres (i.e., minimum propulsion power). Also, the ship could not be able to perform turning manoeuvres when advancing in port beam and stern quartering waves at sea state 6 under low-speed manoeuvres.

The use of Computational Fluid Dynamics (CFD) tools for ship manoeuvring prediction is increasingly gaining popularity with advances in computational power and improved numerical algorithms. Among the applications of CFD in manoeuvring problems, free-running CFD simulations have become a high-fidelity numerical method to evaluate a ship's manoeuvrability due to the importance of viscous and turbulent effects on ship manoeuvring. In the Final Report and Recommendations to the 29th ITTC of the Manoeuvring Committee (ITTC, 2021b), free-running simulations by means of an unsteady Reynolds-Averaged Navier-Stokes (URANS) solver have been stated as a state-of-the-art method for the prediction of a ship's manoeuvring performance. In the framework of CFD-RANS simulations, manoeuvring prediction is conducted using URANS computations coupled with the equations of rigid body motion with full six degrees of freedom (Broglia et al., 2015).

An important early study in this field was due to Muscari et al. (2008), who carried out free-running CFD simulations of a self-propelled twin-screw patrol vessel in deep unrestricted waters by means of the numerical solution of the unsteady RANS equations. They utilised a

Table 2
The simulation cases to which the CFD model is applied.

Model scale (1:75.24)

Case no.	Approach speed U_0 (m/s)	Propeller rev. (RPS)	Wave height H (m)	Encounter Angle μ (degrees)	Encounter Period T_e (s)	Free running manoeuvres
1						
1.1	0.119	3.37	0.0416	180 (Head sea)	1.154	Course keeping control, 35° starboard/port turn
1.2	0.237	4.87	0.0416	180 (Head sea)	1.090	
1.3	0.356	6.35	0.0416	180 (Head sea)	1.033	
2						
2.1	0.109	3.37	0.0416	225 (Bow sea)	1.178	Course keeping control, 35° starboard/port turn
2.2	0.233	4.87	0.0416	225 (Bow sea)	1.128	
2.3	0.346	6.35	0.0416	225 (Bow sea)	1.086	
3						
3.1	0.253	3.37	0.0416	270 (Beam sea)	1.225	Course keeping control, 35° starboard/port turn
3.2	0.368	4.87	0.0416	270 (Beam sea)	1.225	
3.3	0.492	6.35	0.0416	270 (Beam sea)	1.225	
4						
3.1	0.235	3.37	0.0416	315 (Quartering sea)	1.342	Course keeping control, 35° starboard/port turn
3.2	0.351	4.87	0.0416	315 (Quartering sea)	1.408	
3.3	0.479	6.35	0.0416	315 (Quartering sea)	1.489	
5						
5.1	0.276	3.37	0.0416	0 (Following sea)	1.432	Course keeping control, 35° starboard/port turn
5.2	0.391	4.87	0.0416	0 (Following sea)	1.541	
5.3	0.501	6.35	0.0416	0 (Following sea)	1.661	
6						
6.1	0.208	3.37	Calm sea	- (Calm sea)	-	Course keeping control, 35° starboard/port turn
6.2	0.336	4.87	Calm sea	- (Calm sea)	-	
6.3	0.484	6.35	Calm sea	- (Calm sea)	-	

Full scale

Case no.	Approach speed U (m/s)	Propeller rev. (RPS)	Wave height H (m)	Encounter Angle μ (degrees)	Encounter Period T_e (s)	Free running manoeuvres
1						
1.1	1.032 (2.0 knots)	0.39	3.13	180 (Head sea)	10.009	Course keeping control, 35° starboard/port turn
1.2	2.056 (4.0 knots)	0.56	3.13	180 (Head sea)	9.455	
1.3	3.088 (6.0 knots)	0.73	3.13	180 (Head sea)	8.960	
2						
2.1	0.945 (1.8 knots)	0.39	3.13	225 (Bow sea)	10.218	Course keeping control, 35° starboard/port turn
2.2	2.021 (3.9 knots)	0.56	3.13	225 (Bow sea)	9.784	
2.3	3.001 (5.8 knots)	0.73	3.13	225 (Bow sea)	9.420	
3						
3.1	2.195 (4.3 knots)	0.39	3.13	270 (Beam sea)	10.630	Course keeping control, 35° starboard/port turn
3.2	3.192 (6.2 knots)	0.56	3.13	270 (Beam sea)	10.630	
3.3	4.267 (8.3 knots)	0.73	3.13	270 (Beam sea)	10.630	
4						
3.1	2.038 (3.9 knots)	0.39	3.13	315 (Quartering sea)	11.640	Course keeping control, 35° starboard/port turn
3.2	3.044 (5.9 knots)	0.56	3.13	315 (Quartering sea)	12.214	
3.3	4.155 (8.1 knots)	0.73	3.13	315 (Quartering sea)	12.916	
5						
5.1	2.394 (4.7 knots)	0.39	3.13	0 (Following sea)	12.421	Course keeping control, 35° starboard/port turn
5.2	3.391 (6.6 knots)	0.56	3.13	0 (Following sea)	13.366	
5.3	4.346 (8.5 knots)	0.73	3.13	0 (Following sea)	14.407	
6						
6.1	1.804 (3.5 knots)	0.39	Calm sea	- (Calm sea)	-	Course keeping control, 35° starboard/port turn
6.2	2.914 (5.7 knots)	0.56	Calm sea	- (Calm sea)	-	
6.3	4.198 (8.2 knots)	0.73	Calm sea	- (Calm sea)	-	

simplified propeller model to take into consideration the rotating propeller effects on the hydrodynamic forces and moments during ship manoeuvres, by which the turning performance of the ship was estimated. Broglia et al. (2013) studied the turning behaviour of a twin-screw single-rudder model in deep calm water, simulating free-running manoeuvres using an unsteady RANS solver. Approximately 6 million grid cells were generated in their computations, applying a dynamic overlapping grid approach to enable complex

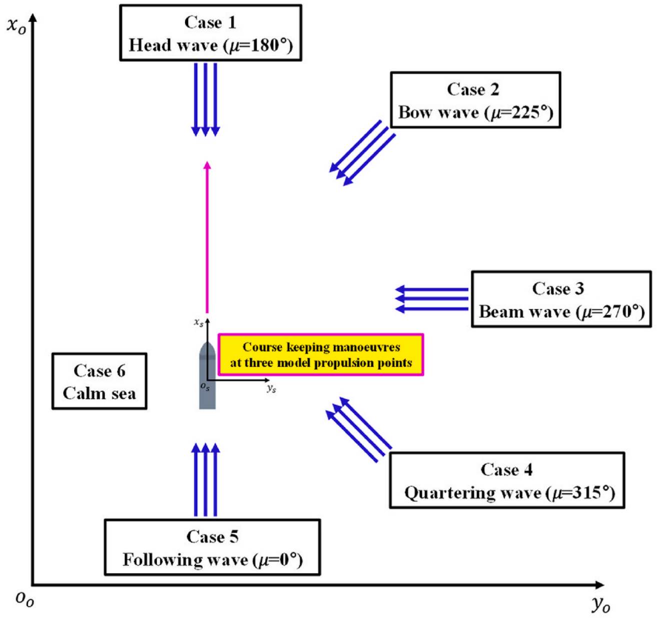

(a) Course keeping manoeuvres

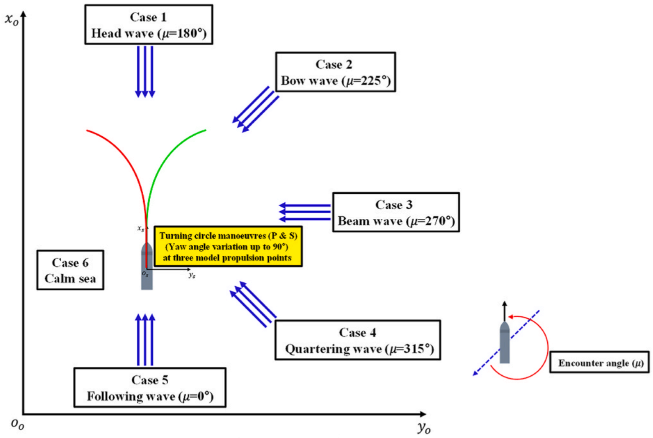

(b) Turning circle manoeuvres

Fig. 3. Schematic views of the simulation cases applied to this study.

geometries and multiple bodies in relative motion to be handled. The flow field interaction between the ship hull and the propeller was modelled based on the actuator disk concept. The effectiveness of free-running CFD simulations was reported by Mofidi and Carrica (2014), who simulated the zigzag manoeuvre of the KCS model in deep calm water using CFDShip-Iowa, which is a piece of general-purpose CFD software developed at the University of Iowa. The numerical results obtained were validated against the available experimental data and were found to be in satisfactory agreement with the experiments, underscoring the reliability of free-running CFD approaches. Subsequently, a series of past research have attempted to apply similar approaches to predict the manoeuvrability of a ship in deep unrestricted water (Broglia et al., 2015; Shen et al., 2015; Dubbioso et al., 2016; Wang et al., 2016; Hasanvand and Hajivand, 2019; Hasanvand et al., 2021; Kim et al., 2021d; Kinaci and Ozturk, 2022), demonstrating that free-running CFD simulations are reliable in estimating the manoeuvring performance of a ship.

As stated above, the studies devoted to free-running CFD simulations in calm water have demonstrated the excellence of the CFD simulations with free-running ship models by showing good agreement between CFD results and the experimental data available. More recently, several researchers have started to focus on the ship's manoeuvrability in various wave conditions by applying the Stokes wave models. The investigation in Wang et al. (2017) was focused on the course-keeping capabilities of the ONR Tumblehome ship model in regular waves by means of an unsteady RANS solver. Their numerical results were compared with the benchmark data in Tokyo 2015 CFD Workshop in ship hydrodynamics and showed good agreement. Afterwards, Wang et al. (2018) and Wang and Wan (2018) utilised the same RANS code, employed in Wang et al. (2017), to perform free-running CFD simulations of zigzag and turning manoeuvres, respectively, for the ONR Tumblehome ship in regular waves. Similar computations were presented in Kim et al. (2021a); Kim et al. (2021b); Kim et al. (2021c); Kim et al. (2022a); Kim and Tezdogan (2022) with various levels of success, where both course-keeping and turning manoeuvres were simulated for the KCS model in a wide range of wave conditions by means of an unsteady RANS method.

As can be seen from the guideline proposed by the MEPC (IMO, 2021), an increasing demand for understanding the manoeuvrability of a ship with minimum propulsive power in adverse weather conditions has drawn more and more attention from academic and industrial researchers. Nevertheless, due to its brevity, a very limited number of studies dedicated to understanding the manoeuvring performance of a ship with low advance speeds in adverse sea states exist in the open literature (for example, the SHOPERA project and Kim et al. (2022d)). It is no wonder that the manoeuvring behaviour of a ship can significantly vary depending on various ship types and geometries. Thus, this paper was motivated to evaluate the manoeuvrability of the KRISO Container Ship (KCS) model with low advance speeds in adverse weather conditions, which is the benchmark ship hull but not examined in this field study. The main novelty of this study lies in demonstrating the contribution of low advance speeds to the manoeuvring performance of a ship (such as course-keeping and turning manoeuvres) in adverse weather conditions, by means of an unsteady RANS solver.

In the present paper, a series of free-running CFD simulations were systematically carried out for the KCS model advancing forward in adverse weather conditions. The particular focus of this work lies in the course-keeping and turning circle manoeuvres at low speeds. In order to provide a better interpretation of the manoeuvring response, both hydrodynamic forces and moments acting on the ship performing a self-propelled free manoeuvre are discussed along with kinematic parameters and ship trajectories.

The remainder of this paper will continue by illustrating the research methodology for the free-running CFD simulation in Section 2, with a detailed description of the numerical scheme in the contained subsections. Then, all of the CFD results and their analysis are provided in Section 3. Finally, the main results drawn from this work are summarised in Section 4, along with recommendations for future avenues of research.

2. Methodology

The research methodology towards the investigation on the manoeuvring performance of the ship with low advance speeds in adverse weather conditions is shown in this section, along with a detailed description of the procedure in the included sub-sections. As presented in Fig. 1, the research procedure is composed of four steps: *1) goal and scope, 2) numerical modelling, 3) execution of free running simulations, and 4) results of analysis*. The overall research goal and the selection of the analysis scope are dealt with in the first step. The scope of numerical simulations should be sufficiently well defined to represent the general observations on the relation between the variable factors selected and the manoeuvring behaviour of the ship. Given the scope of the analysis, the numerical setup of a free-running CFD model is performed in the second step. Special care is needed when carrying out numerical modelling tasks. In this regard, the governing equations to be solved should be first adopted to solve turbulent flows around the ship. In addition to this, mesh resolution, defining the time step, boundary conditions, etc., should be taken into consideration when developing a

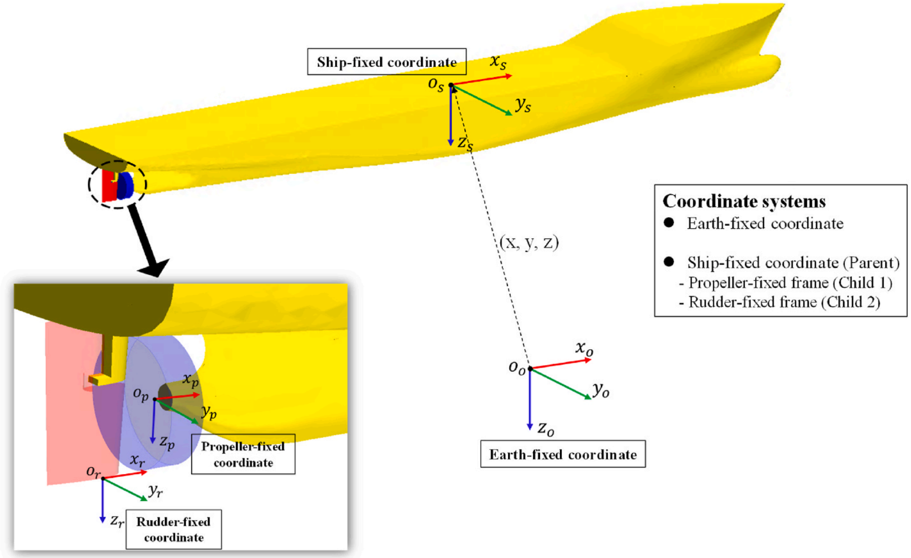

Fig. 4. The coordinate systems used in this study, adapted from Kim and Tezdogan (2022).

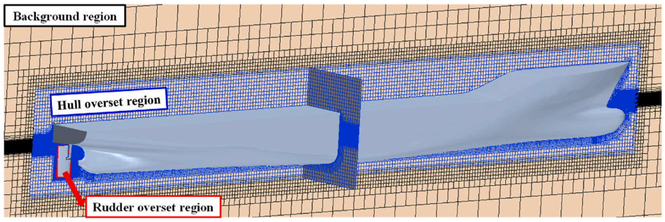

Fig. 5. Mesh structure of the computational domain in a typical free running CFD model.

free-running CFD model. In the third step, the self-propulsion computation in a given environmental condition should be first carried out to reach the target surge speed. Then, course-keeping and turning circle manoeuvres are performed to identify the manoeuvring performance of the ship with low advance speeds in adverse weather conditions. In the fourth step, all of the results obtained from the numerical simulations including the important hydrodynamic features, the critical manoeuvring indices, and relevant flow fields are demonstrated and discussed in detail.

2.1. Step 1: Goal and scope

The primary goal of this paper is to provide a practical insight into the manoeuvring performance of a ship with low advance speeds in adverse weather conditions. To this purpose, a systematic investigation on the manoeuvrability of a ship performing low-speed free-running manoeuvres in adverse weather conditions using CFD was conducted.

In this work, all the free-running simulations were performed for the KRISO Container Ship (KCS) model with a scale factor of 75.24, which is

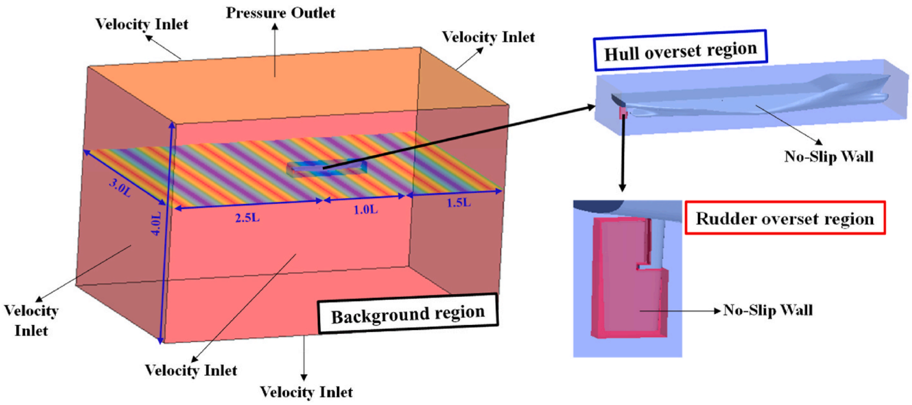

Fig. 6. The schematic view of the computational domain with the applied boundary conditions.

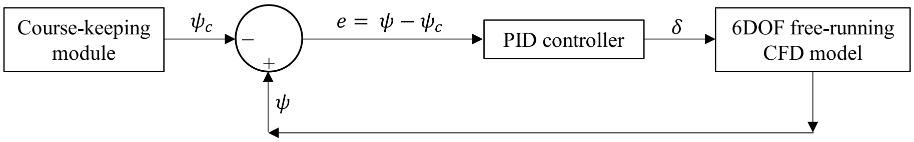

Fig. 7. The block diagram of the autopilot applied to the CFD model for the course-keeping manoeuvre.

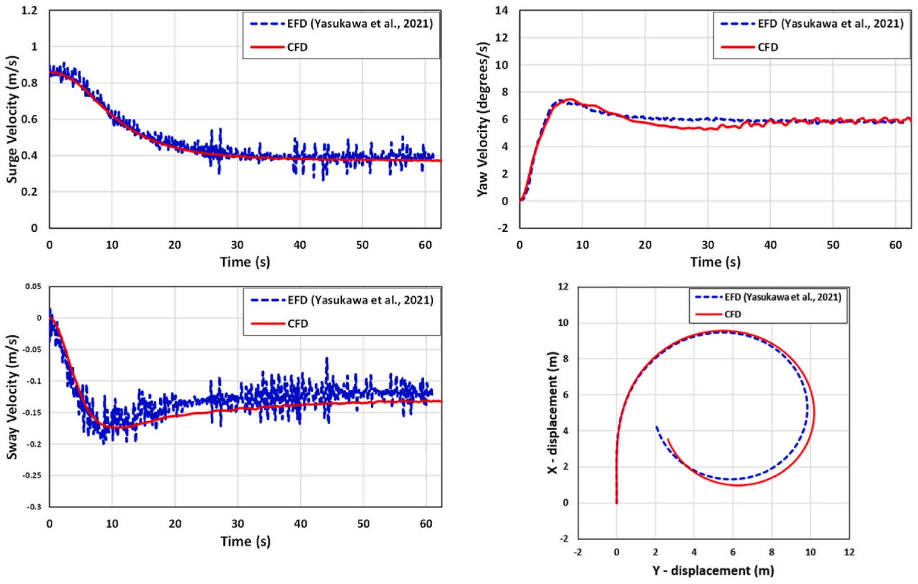

(a) Calm water

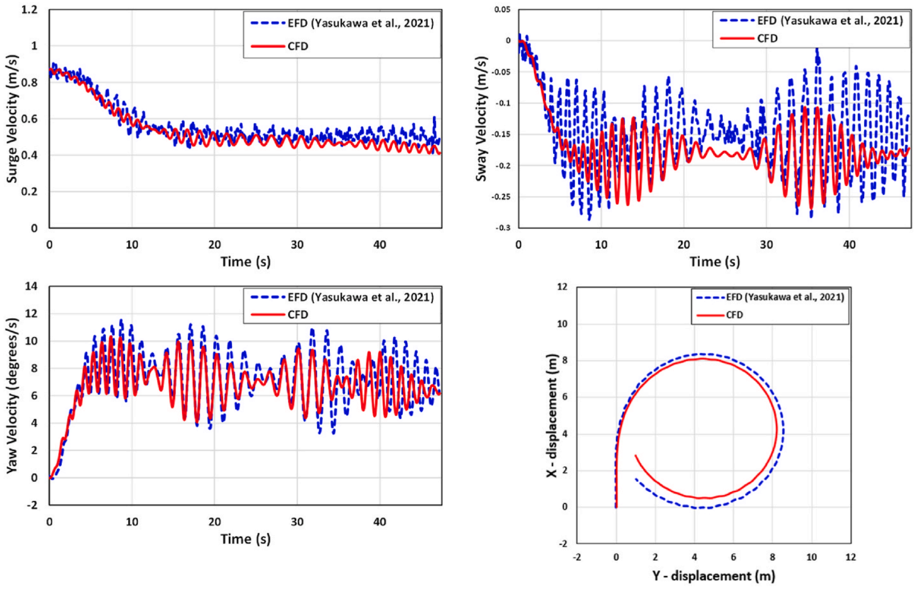

(b) Regular head waves

Fig. 8. The comparison of the trajectory and kinematic parameters experienced by the ship performing turning manoeuvres in calm water and regular head waves, adapted from Kim et al. (2021c).

one of the benchmark hull forms. Fig. 2 depicts the geometry of the ship characterised by a traditional single rudder/single propeller configuration, and the main properties of the model are reported in Table 1. The CFD simulations were carried out at eighteen different conditions, as presented in Table 2 and Fig. 3, each indicated by their case numbers. The encounter frequency of the wave, ω_e, is calculated as $\omega_e = \omega[1 - (\omega U \cos\mu)/g]$, where ω is the wave frequency, U is the ship forward speed, μ is the ship's heading angle relative to the wave direction, and g denotes the gravitational acceleration. Considering the guidelines by IMO (2021), the model propulsion point corresponding to the full-scale speed of 2.0 knots in head waves was applied to the free-running CFD model (3.37 RPS). Additional two model propulsion points (4.87 and 6.35 RPS) corresponding to the full-scale speeds of 4.0 and 6.0 knots in head waves were also considered with a view to identifying the contribution of the propulsion power to the manoeuvrability of the ship. Kim et al. (2022d) experimentally demonstrated that the manoeuvring performance of a ship in regular waves is similar to that in irregular waves in case the regular waves have the same mean height and the energy period of irregular waves. Given this, the regular waves characterised by the height and period equivalent to the same mean height and the energy period of the irregular waves representing sea state 6 were applied in this work. The reason for selecting the regular waves in this work is that the time to complete the free-running CFD simulation of irregular waves takes approximately six times longer than that of regular waves, as shown in Kim et al. (2021c); Kim and Tezdogan (2022). As for the regular waves cases (Cases 1.1–5.3), a fifth-order Stokes wave model was used to generate regular waves with a wave height of 0.0416m and a period of 1.225s in model scale (the wavelength to ship length ratio

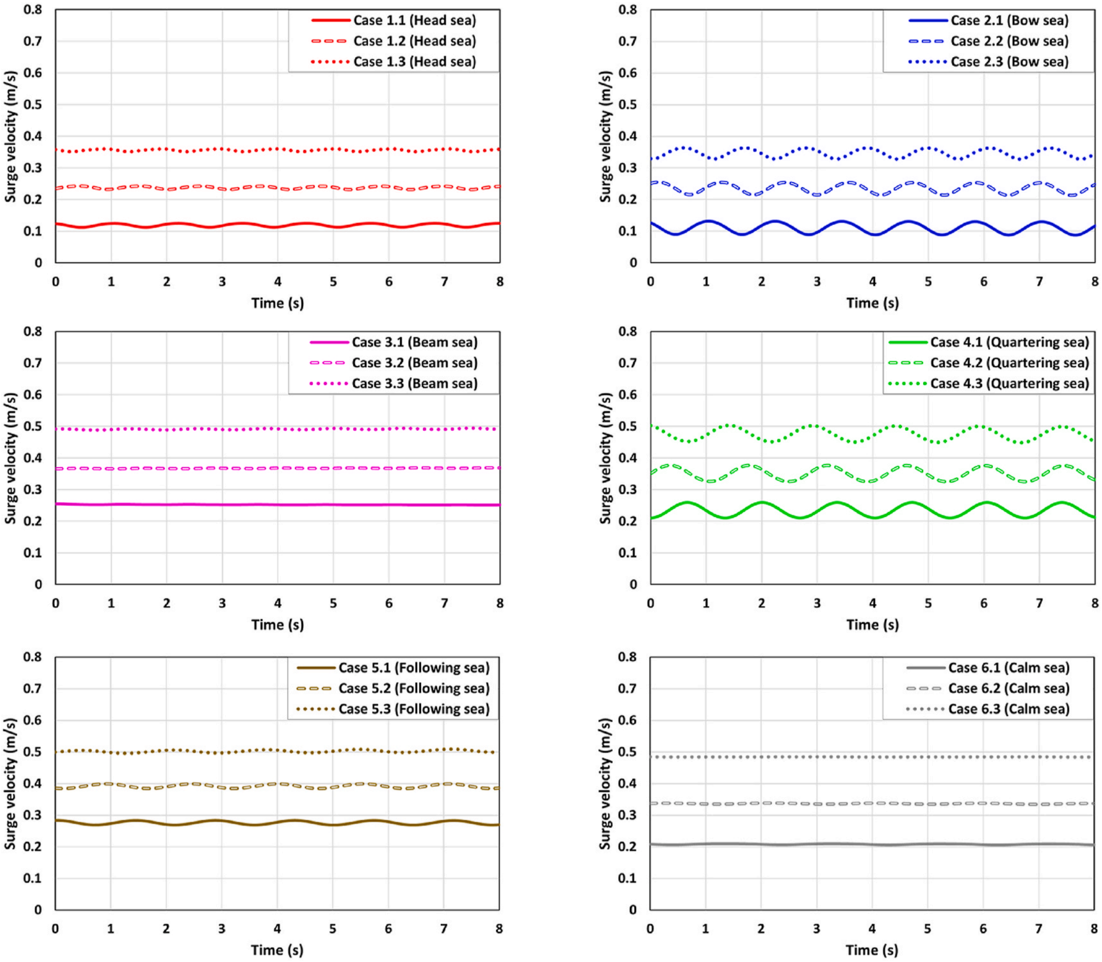

(a) Approach speed

Fig. 9. The time histories of the a) approach speed, b) ship resistance, c) pitch motion, and d) heave motion for all the cases.

$\lambda/L_{BP} = 0.77$). These values correspond to a mean wave height of 3.13m and an energy period of 10.63s for the sea state 6 in an irregular seaway, as reported in Kim et al. (2022d). The wave incident angles were selected to cover the whole range of main wave directions as follows: *1) Head sea, 2) Bow sea, 3) Beam sea, 4) Quartering sea, 5) Following sea*. It should be highlighted that the following three manoeuvres were performed per each case: *1) Course keeping control, 2) 35° starboard turning manoeuvres,* and *3) 35° port turning manoeuvres*. All the free-running simulations performed in this work were subjected to deep water conditions.

2.2. Step 2: Numerical modelling

In this work, the free-running CFD simulations were implemented utilising the commercial CFD code STAR-CCM+ (version 15.04) developed by Siemens PLM Software. The detailed description of the numerical setup used in this work is presented in the following subsections.

2.2.1. Governing equations

An Unsteady Reynolds-Averaged Navier-Stokes (URANS) approach was adopted to compute turbulent flows around the ship performing a self-propelled manoeuvre. The mass and momentum conservation equations for unsteady incompressible flows are expressed in vectorial form as follows:

$$\nabla \cdot \mathbf{U} = 0 \tag{1}$$

$$\frac{\partial(\rho\mathbf{U})}{\partial t} + \nabla \cdot \left[\rho\left(\mathbf{U} - \mathbf{U}_g\right)\mathbf{U}\right] = -\nabla p + \nabla \cdot \left(\mu_{eff}\nabla\mathbf{U}\right) + \nabla\mathbf{U}\cdot\nabla\mu_{eff} + q_i \tag{2}$$

where $\nabla\cdot(\cdot)$ and $\nabla(\cdot)$ represent the divergence and gradient operators, respectively. $\mathbf{U}$ is the fluid velocity and $\mathbf{U}_g$ is the grid velocity; p is the static pressure; ρ is the fluid density; $\mu_{eff} = \rho(\nu + \nu_t)$ indicates the effective dynamic viscosity, where ν and ν_t stand for the kinematic and eddy viscosity, respectively (ν_t is obtained from the turbulence model); q_i is a user-defined source term.

The turbulence model selected in this study was the Menter's Shear Stress Transport (SST) model (Menter, 1994) for the closure of the governing equations. The SST turbulence model is a two-equation eddy viscosity turbulence model which utilises the original k−ω turbulence model of Wilcox in the inner region of the boundary layer and switches to the standard k-ε turbulence model in the far-field. The transformation of the two turbulence models can be achieved using blending functions depending on the turbulence length scale. This turbulence model is one of the most widely and successfully used turbulence models to perform free-running CFD simulations in the open literature (Mofidi and Carrica, 2014; Carrica et al., 2016; Wang and Wan, 2018; Wang et al., 2018; Kim et al., 2021c, 2022c). The first closure equation (Eq. (3)) is the transport equation for the turbulent kinetic energy k, while the second one (Eq. (4)) is the transport equation for the specific dissipation rate ω. The SST turbulence model is given by:

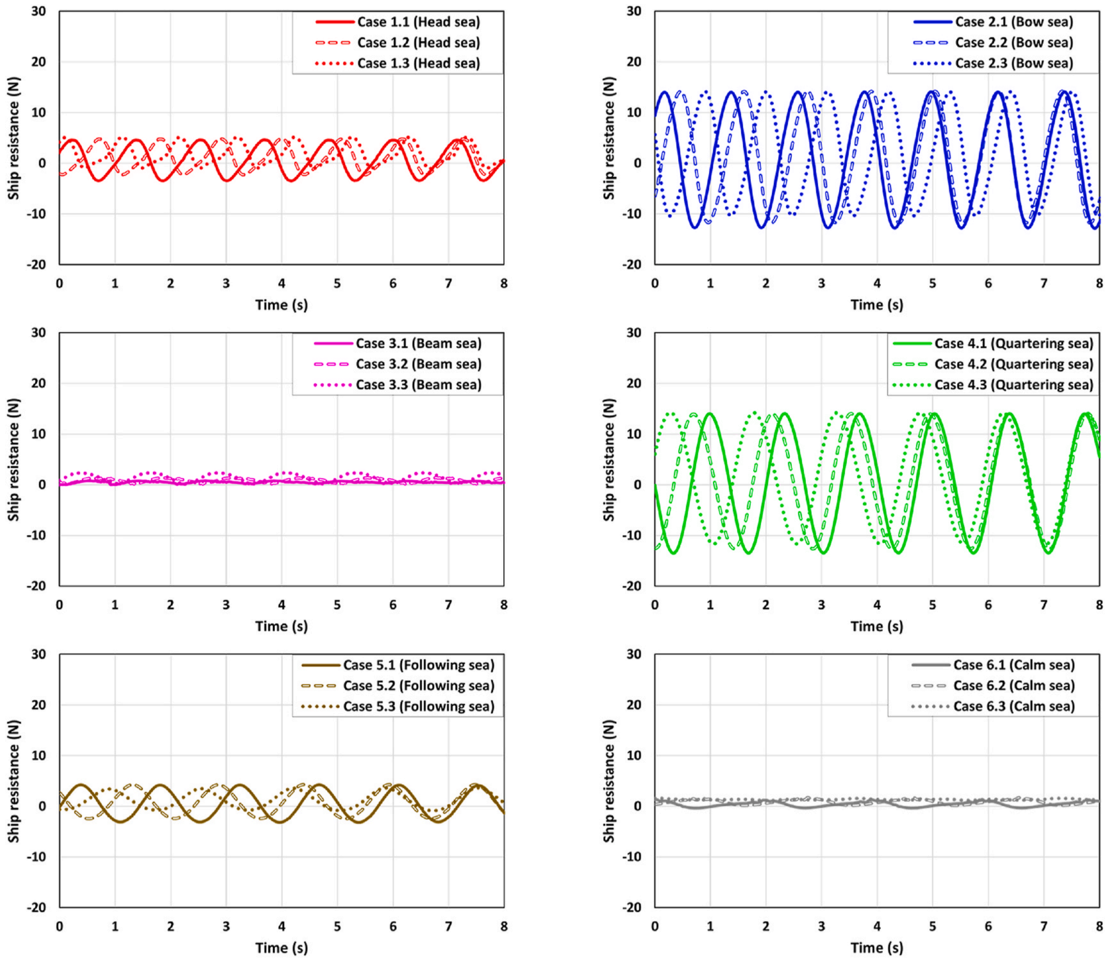

(b) Ship resistance

Fig. 9. (*continued*).

$$\frac{\partial(\rho k)}{\partial t}+\nabla\cdot(\rho k\mathbf{U})=\left[\mu_t\left(\nabla\mathbf{U}+(\nabla\mathbf{U})^{\mathrm{T}}-\frac{2}{3}\nabla\cdot\mathbf{U}\right)-\frac{2}{3}\rho k\delta_{i,j}\right]\nabla\mathbf{U}-\beta^{*}\rho\omega k+\nabla\cdot[(\mu+\sigma_k\mu_t)\nabla k] \tag{3}$$

$$\frac{\partial(\rho\omega)}{\partial t}+\nabla\cdot(\rho\omega\mathbf{U})=\frac{\gamma}{\nu_t}\left[\mu_t\left(\nabla\mathbf{U}+(\nabla\mathbf{U})^{\mathrm{T}}-\frac{2}{3}\nabla\cdot\mathbf{U}\right)-\frac{2}{3}\rho k\delta_{i,j}\right]\nabla\mathbf{U}-\beta\rho\omega^2+\nabla\cdot[(\mu+\sigma_\omega\mu_t)\nabla\omega]+2\rho(1-F_1)\frac{\sigma_{\omega2}}{\omega}\nabla k\cdot\nabla\omega+\nabla\cdot[(\mu+\sigma_\omega\mu_t)\nabla\omega]+2\rho(1-F_1)\frac{\sigma_{\omega2}}{\omega}\nabla k\cdot\nabla\omega \tag{4}$$

in which the first blending function F_1 is defined as $F_1=\tanh\left\{\left[\min\left(\max\left(\frac{\sqrt{k}}{0.09\omega y};\frac{500\upsilon}{y^2\omega}\right);\frac{4\rho\sigma_{\omega2}k}{CD_{k\omega}y^2}\right)\right]^4\right\}$ with $CD_{k\omega}=\max\left(\frac{2\rho\sigma_{\omega2}}{\omega}\nabla k\cdot\nabla\omega;10^{-20}\right)$. y indicates the distance from the nearest wall. The eddy-viscosity coefficient in the SST model is defined as $\mu_t(=\rho\nu_t)=\frac{\rho a_1 k}{\max(a_1\omega;\Omega F_2)}$ where Ω is the absolute value of the vorticity and F_2 is the second blending function defined by $F_2=\tanh\left\{\left[\max\left(2\frac{\sqrt{k}}{0.09\omega y};\frac{500\upsilon}{y^2\omega}\right)\right]^2\right\}$ The constants Φ (β^*, β, σ_k, σ_ω, $\cdots$) of the turbulence model are calculated from the constants, Φ_1,Φ_2, as follows: $\Phi=F_1\Phi_1+(1-F_1)\Phi_2$. The SST closure constants of the formulas can be found in Menter (1994) for details.

The Volume of Fluid (VOF) method was adopted in this work to capture unsteady three-dimensional free-surface flows around the ship in either a flat or regular wave (Kavli et al., 2017; Song et al., 2020; Terziev et al., 2020; Kim et al., 2022b). The VOF transport equation can be expressed as (Siemens, 2020):

$$\frac{\partial\alpha_i}{\partial t}+\nabla\cdot\left[\alpha_i\left(\mathbf{U}-\mathbf{U}_g\right)\right]=S_{\alpha_i}-\frac{\alpha_i}{\rho_i}\frac{D\rho_i}{Dt}-\frac{1}{\rho_i}\nabla\cdot\left(\alpha_i\rho_i\mathbf{v}_{d,i}\right) \tag{5}$$

where α_i represents the volume fraction of phase i and its value varies from 0 to 1 to describe the relative proportion of fluid in each cell ($\alpha=0$: air, $0<\alpha<1$: two-phase interface, $\alpha=1$: water). S_{α_i} is a user-defined source term of phase i; $\frac{D\rho_i}{Dt}$ is the Lagrangian derivative of the phase densities ρ_i; $\mathbf{v}_{d,i}$ is the diffusion velocity. The VOF approach has remarkable advantages in treating complex interface evolutions, even

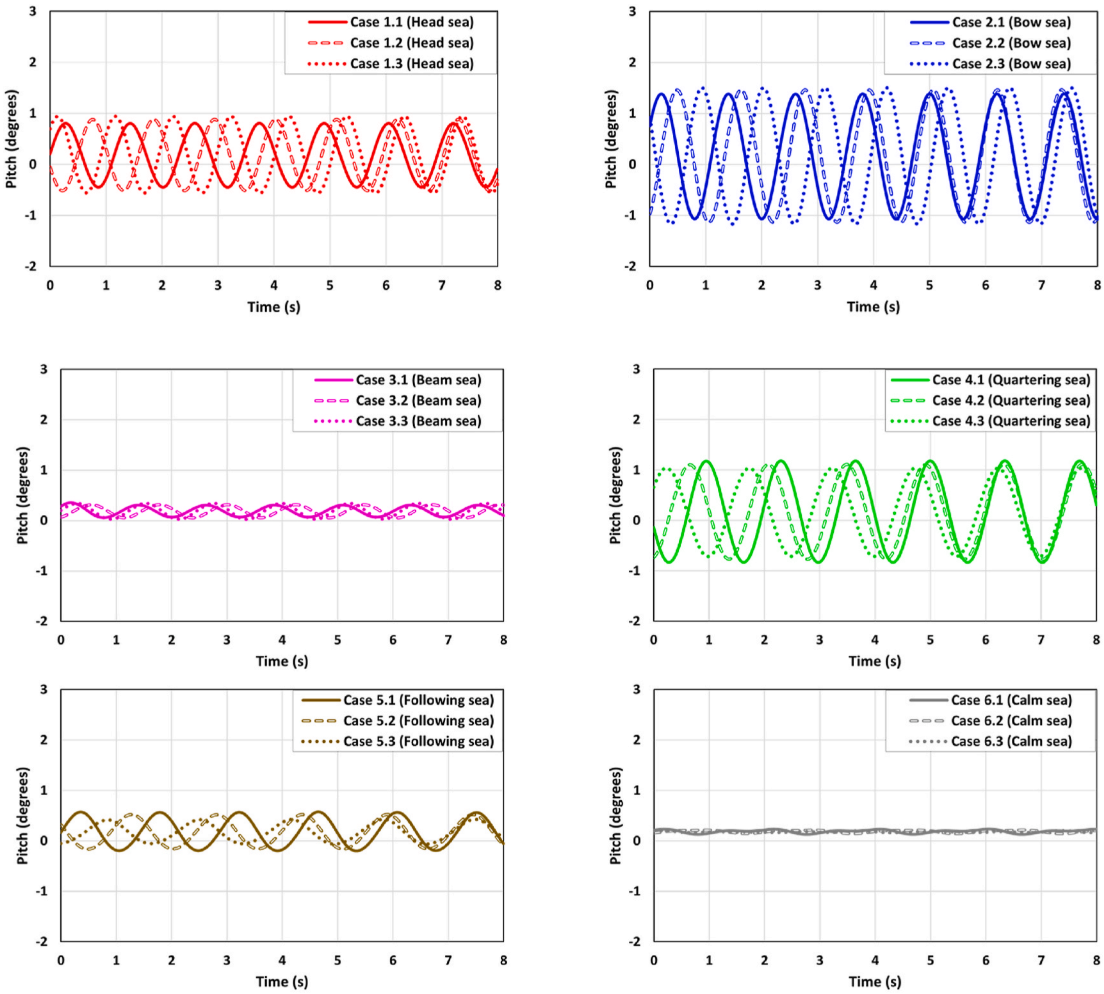

(c) Pitch displacement

Fig. 9. (*continued*).

breaking and reconnecting surfaces, and in its mass conservation properties, as stated in Di Mascio et al. (2007). As reported in Perić and Abdel-Maksoud (2018), the source terms for the momentum equation (q_i) and the VOF transport equation (S_{α_i}) can be used to enable undesired wave reflections occurring at domain boundaries to be prevented. The VOF method has been widely adopted in the literature to position the free surface (Tezdogan et al., 2016; Kavli et al., 2017; Terziev et al., 2020; Kim et al., 2021c).

In this study, the RANS-VOF solver employed uses a finite volume method that discretises the integral formulation of the Navier-Stokes equations. The temporal discretisation is based on a second-order implicit backward Euler scheme for the transient terms in the RANS formulae. The convection terms and diffusive terms in the governing equations were discretised by applying a second-order upwind scheme and a second-order centred scheme, respectively. The pressure–velocity coupling is realised by means of a SIMPLE-type algorithm.

2.2.2. *Body-force method*

The average effect of the propeller rotating behind the hull of a ship was simulated by means of an actuator disk model based on the body-force method. The main properties of the actuator disk model are only briefly explained here; the interested reader is referred to Kim et al. (2021b) and Kim et al. (2022a) for details. A number of input variables, such as the open water curves and the geometric features, are required to be entered into the STAR-CCM + software when modelling an actuator disk. The thrust and torque induced by the actuator disk are computed at each time step from the open water characteristics, taking into account the volume-averaged velocity over the inflow velocity plane located upstream of the disk. In other words, axial and tangential body forces are distributed at each time step over an actuator disk of finite thickness following the body-force method to estimate the flow field induced by the mutual interactions between the hull, the propeller, and the rudder (Siemens, 2020). In the authors' previous studies (Kim et al., 2021c, 2022c), the actuator disk model designed to represent the KCS propeller was taken into account when performing the free-running simulations of the KCS in deep unrestricted water, waves, and shallow water, exhibiting promising results.

2.2.3. *Coordinate systems*

Four frames of reference were taken into account for the free-running CFD model, as presented in Fig. 4:

- Earth-fixed coordinate frame ($o_o - x_o y_o z_o$): an inertial frame of reference centred at the pivot point (o_o) of the computational domain. When the simulation is initialised, the x_o-axis is orthogonal to the transverse plane of the ship (directed towards the bow), the y_o-axis is orthogonal to the longitudinal plane (directed towards the starboard), and the z_o-axis is oriented to complete a right-handed orthogonal frame (positive downwards).
- Ship-fixed coordinate frame (o_s - $x_s y_s z_s$): a moving frame of reference centred at the centre of mass of the ship. The x_s-axis is parallel to the ship's longitudinal axis (positive forward), the y_s-axis is parallel to

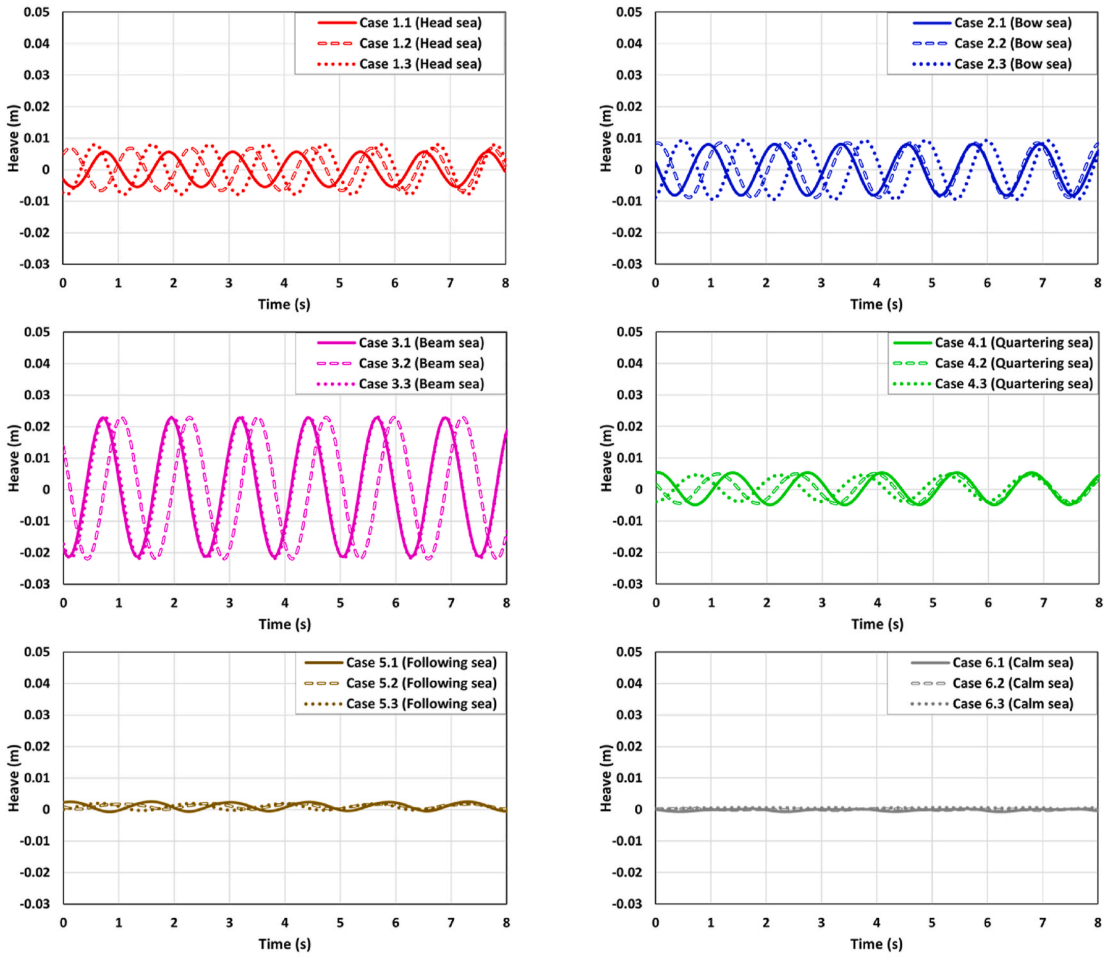

(d) Heave displacement

Fig. 9. (*continued*).

the ship's transverse axis (positive starboard side), the z_s-axis is directed towards downward.

- Propeller-fixed coordinate frame *(o_p - $x_py_pz_p$)*: a moving frame of reference centred at the propeller hub. The x_p-axis indicates the propeller axis of revolution. The thrust force generated by the actuator disk is applied in the x_p-axis direction.
- Rudder-fixed coordinate frame *(o_r - $x_ry_rz_r$)*: a moving frame of reference centred at the bottom of the rudder on the Aft Perpendicular (AP). The z_r-axis is oriented along the rudder axis of rotation; the positive sign of the rudder angle means rudder deflection to the port side.

In this study, in order to simulate the realistic behaviour of the ship performing free manoeuvres, the Dynamic Fluid Body Interaction (DFBI) approach was adopted to couple the equations of rigid body motion with full six degrees of freedom with the unsteady RANS equations (Siemens, 2020). In the inertial frame of reference, the hydrodynamic forces and moments acting on the ship are calculated by solving the RANS equations for the fluid flow. Then, 6 DOF motion equations in the non-inertial ship-fixed coordinate system are solved to determine the new position and attitude of the ship during manoeuvres.

2.2.4. *Mesh generation*

The built-in automated meshing tool in STAR-CCM+ was adopted for mesh generation, which uses the Cartesian cut-cell method. Two different mesh generations were applied for the free-running simulation (Cases 1.1–5.3: regular waves, and Cases 6.1–6.3: calm water), resulting in a computation mesh of circa 13 and 6 million cells in total, respectively. A trimmed cell mesher was selected to generate the volume mesh, for its good ability to produce a high-quality grid for complex mesh generating problems. The resulting mesh was composed dominantly of unstructured hexahedral cells with trimmed cells next to the ship model. A surface remesher was used to generate a high-quality surface mesh, optimising the geometry surface during volume meshing. With an aim to improve the accuracy of the numerical solution near the surface boundary layer, a prism layer mesh model was applied to generate six layers of orthogonal prismatic cells adjacent to the ship hull surfaces. The most significant changes in the flow are expected in the stern region of the ship performing a self-propelled manoeuvre. It is the region where the complex interactions between the propeller and rudder occur during manoeuvres. The numerical computation therefore should be capable of capturing as many detailed flow properties as possible, and thus a local grid refinement was made in the vicinity of the stern. Additional refinements were applied to give finer grids in the areas around the bow, the tight gap parts between the rudder blade and horn, and the free surface region for the accuracy of capturing the flow features. It has to be mentioned that 80 grid points per wavelength (in the x and y directions, horizontal directions) and 20 grid points per wave height (in the z direction, vertical direction) were generated on the free surface to avoid wave dissipation for the wave simulations (Cases 1.1–5.3), according to ITTC (2011). The free-running CFD model in waves was selected to exhibit the final computational domain mesh, as presented in Fig. 5. A dynamic overlapping grid approach was applied to handle the complex motions of the ship performing a self-propelled manoeuvre, resulting in

Table 3
Fourier series analysis of the approach speed, ship resistance, pitch motion, and heave motion experienced by the ship performing the course-keeping manoeuvres.

	Case 1 (Head sea)			Case 2 (Bow sea)		
	Case 1.1	Case 1.2	Case 1.3	Case 2.1	Case 2.2	Case 2.3
Approach speed U_0						
0th FS term (m/s)	0.119	0.237	0.356	0.109	0.233	0.346
Resistance F_X						
0th FS term (N)	0.597	1.007	1.753	0.833	1.235	1.630
1st FS term (N)	3.906	3.283	2.720	13.344	12.578	11.719
Pitch displacement						
0th FS term (degrees)	0.175	0.151	0.184	0.190	0.166	0.160
Non-dimensionalised 0th FS term	19.786	17.072	20.803	21.482	18.768	18.089
1st FS term (degrees)	0.630	0.692	0.767	1.125	1.274	1.290
Non-dimensionalised 1st FS term	71.229	78.238	86.719	127.195	144.041	145.850
Heave displacement						
0th FS term (m)	0.000	0.000	0.000	0.000	0.000	0.000
Non-dimensionalised 0th FS term	0.000	0.000	0.000	0.000	0.000	0.000
1st FS term (m)	0.0056	0.0068	0.0080	0.0077	0.0085	0.0091
Non-dimensionalised 1st FS term	0.2692	0.3269	0.3846	0.3702	0.4087	0.4375
	Case 3 (Beam sea)			Case 4 (Quartering sea)		
	Case 3.1	Case 3.2	Case 3.3	Case 4.1	Case 4.2	Case 4.3
Approach speed U_0						
0th FS term (m/s)	0.253	0.368	0.492	0.235	0.351	0.479
Resistance F_X						
0th FS term (N)	0.535	0.852	1.401	0.377	1.082	2.067
1st FS term (N)	0.230	0.465	1.156	13.745	13.500	13.302
Pitch displacement						
0th FS term (degrees)	0.193	0.186	0.188	0.161	0.190	0.206
Non-dimensionalised 0th FS term	21.821	21.029	21.256	18.203	21.482	23.291
1st FS term (degrees)	0.140	0.140	0.173	1.016	0.948	0.910
Non-dimensionalised 1st FS term	15.829	15.829	19.560	114.871	107.183	102.886
Heave displacement						
0th FS term (m)	0.000	0.000	0.000	0.000	0.000	0.000
Non-dimensionalised 0th FS term	0.000	0.000	0.000	0.000	0.000	0.000
1st FS term (m)	0.0220	0.0223	0.0223	0.0050	0.0045	0.0041
Non-dimensionalised 1st FS term	1.0576	1.0721	1.0721	0.2404	0.2163	0.1971
	Case 5 (Following sea)			Case 6 (Calm sea)		
	Case 5.1	Case 5.2	Case 5.3	Case 6.1	Case 6.2	Case 6.3
Approach speed U_0						
0th FS term (m/s)	0.276	0.391	0.501	0.208	0.336	0.484
Resistance F_X						
0th FS term (N)	0.565	0.761	1.277	0.414	0.820	1.303
1st FS term (N)	3.642	3.262	2.208	-	-	-
Pitch displacement						
0th FS term (degrees)	0.190	0.168	0.177	0.188	0.185	0.178
Non-dimensionalised 0th FS term	21.482	18.994	20.012	-	-	-
1st FS term (degrees)	0.394	0.328	0.245	-	-	-
Non-dimensionalised 1st FS term	44.546	37.084	27.700	-	-	-
Heave displacement						
0th FS term (m)	0.000	0.000	0.000	0.000	0.000	0.000
Non-dimensionalised 0th FS term	0.000	0.000	0.000	-	-	-
1st FS term (m)	0.0015	0.0007	0.0011	-	-	-
Non-dimensionalised 1st FS term	0.0721	0.0336	0.0528	-	-	-

three different regions of the computational domain for the present numerical model (as seen in Fig. 5): *1) background region, 2) hull overset region,* and *3) rudder blade overset region.* The major advantage of the overlapping grid approach lies in enabling overset regions (i.e., multiple bodies) to move independently without any constraints while guaranteeing a high-quality grid. It should be highlighted that the use of overlapping grids made it possible to simulate the full 6 DOF motions of the ship as well as the deflection of the rudder blade according to the prescribed control mechanisms.

2.2.5. *Determination of the time step*

It should be stated that ITTC (2011) recommends at least 100 time

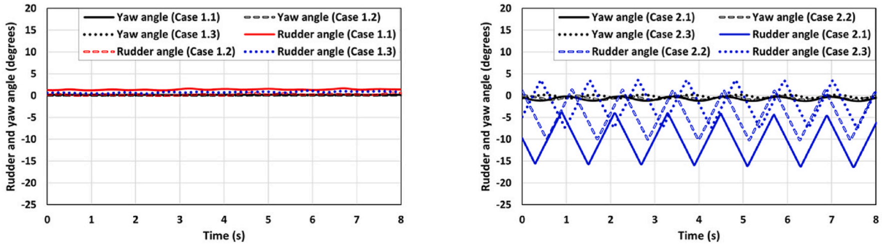

(a) Case 1 (Head sea) (b) Case 2 (Bow sea)

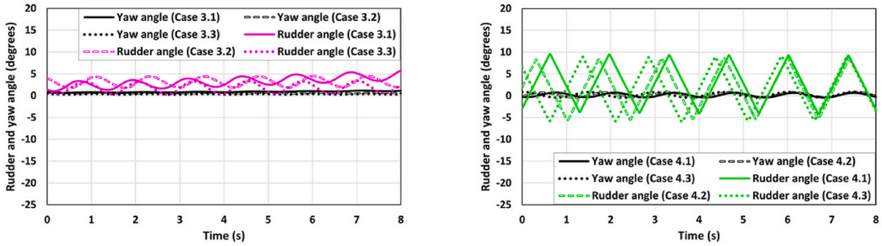

(c) Case 3 (Beam sea) (d) Case 4 (Quartering sea)

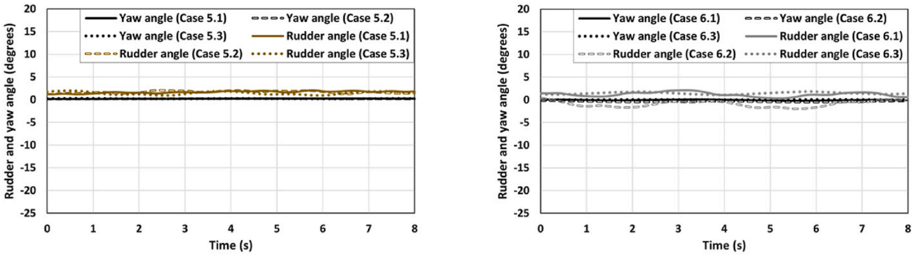

(e) Case 5 (Following sea) (f) Case 6 (Calm sea)

Fig. 10. The time histories of the yaw angle and rudder deflection angle experienced by the ship during the course-keeping manoeuvre for all the cases.

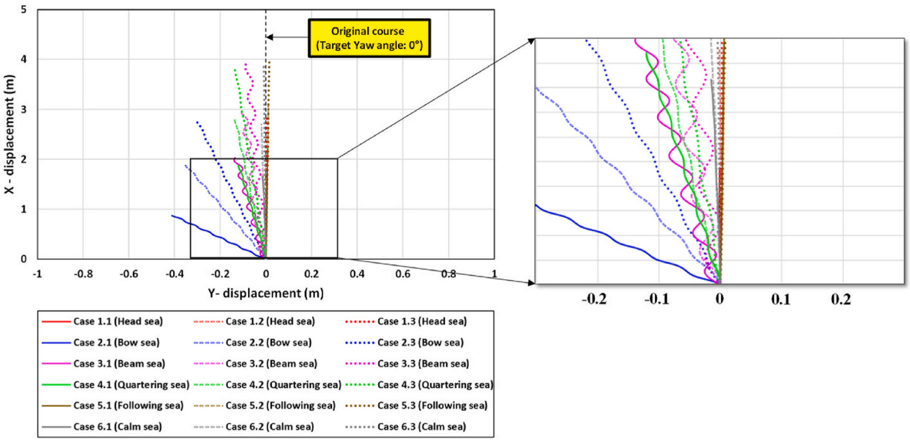

Fig. 11. The comparison of the predicted trajectories for all the cases.

steps per encounter period for regular wave simulations, in order to enable the desired wave propagation to be guaranteed during the simulation. The time-step size of 0.005s was selected throughout all the simulations, which is two times lower than the recommendation of ITTC (2011).

2.2.6. *Computational domain and boundary conditions*

The boundary conditions of the simulations performed in this work were chosen to represent the ship model performing self-propelled manoeuvres in regular waves or calm water. Fig. 6 displays the schematic view of the domain with the KCS model appended with a semi-balanced rudder and the selected boundary conditions. The upstream, downstream, side, and bottom boundaries of the domain were modelled as a velocity inlet boundary condition to avoid a velocity gradient between the fluid and wall. The initial characteristics of the flow at all inlet boundaries were set to the properties of the regular wave or the flat wave to be simulated, i.e., wave height, period/length, and direction. Hence, the stable propagation of the wave with specific characteristics could be attained in the computational domain during the simulation. A pressure outlet boundary condition was set to the top boundary. As expected, the KCS hull and rudder blade were both modelled as no-slip boundary conditions. Undesired wave reflections at the domain boundaries in flow simulations with free-surface waves should be minimised to avoid large errors in the results. To this purpose, the VOF

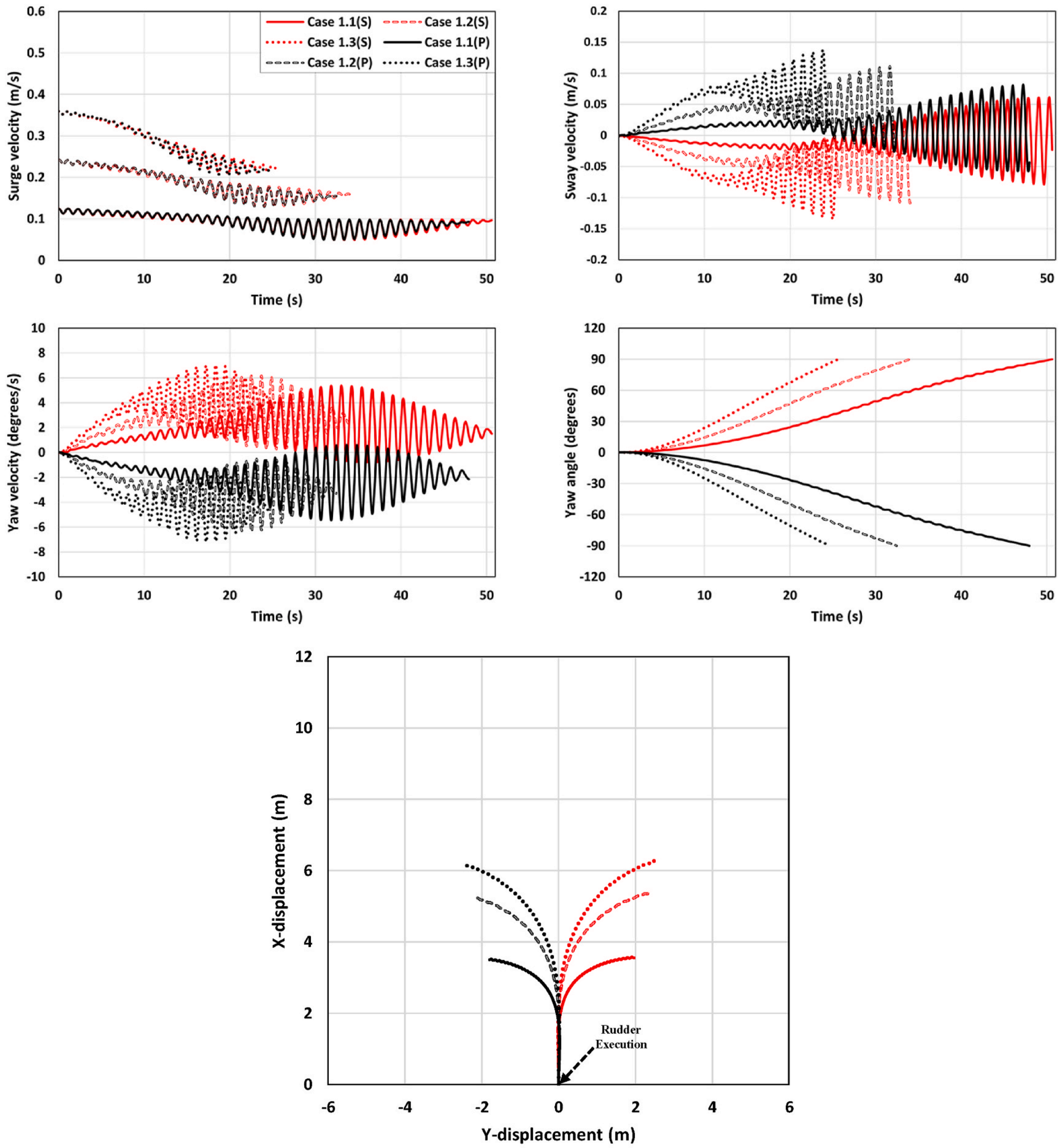

(a) Case 1 (Head sea)

Fig. 12. The time histories of the ship velocities, yaw angles, and trajectories during the turning manoeuvre for all cases (S: starboard turn, P: port turn).

wave forcing capability of the software (Choi and Yoon, 2009) was applied to the boundaries at the upstream, downstream, and sides for the wave simulations (Cases 1.1–5.3), whereas the VOF wave damping capability was applied to the same vertical boundaries for the calm water simulations (Cases 6.1–6.3). The VOF wave forcing and damping length were set to be 1.0 LBP (~3.06 m), based on the recommendations and applications reported in Siemens (2020). It is important to highlight that each computational region utilised different motion capabilities for the free-running simulation. The hull overset region was constructed to move in all degrees of freedom based on the DFBI module, while the rudder overset region was designed to follow the ship and to be controlled according to the prescribed controllers. The background region was defined to only follow the horizontal motions of the ship (i.e., surge, sway, and yaw motions) with an aim to ensure the desired wave propagation.

2.2.7. *Control mechanism*

Two different types of ship manoeuvres were taken into account in this study: *1) course keeping control* and *2) turning circle manoeuvre (35° starboard/port turn)*.

When it comes to the course keeping control, the following control module was constructed to assess the course-keeping capability of the ship:

$$\delta(t) = K_p e(t) + K_i \int_0^t e(t)dt + K_d \frac{de(t)}{dt} \tag{6}$$

$$e(t) = \psi(t) - \psi_c \tag{7}$$

where t representing the time (s) elapsed after the start of the ship manoeuvre, $\delta(t)$ the rudder angle (°), $\psi(t)$ the instantaneous yaw angle (°) at a given time, ψ_c the target yaw angle (°) which was set at 0° to keep

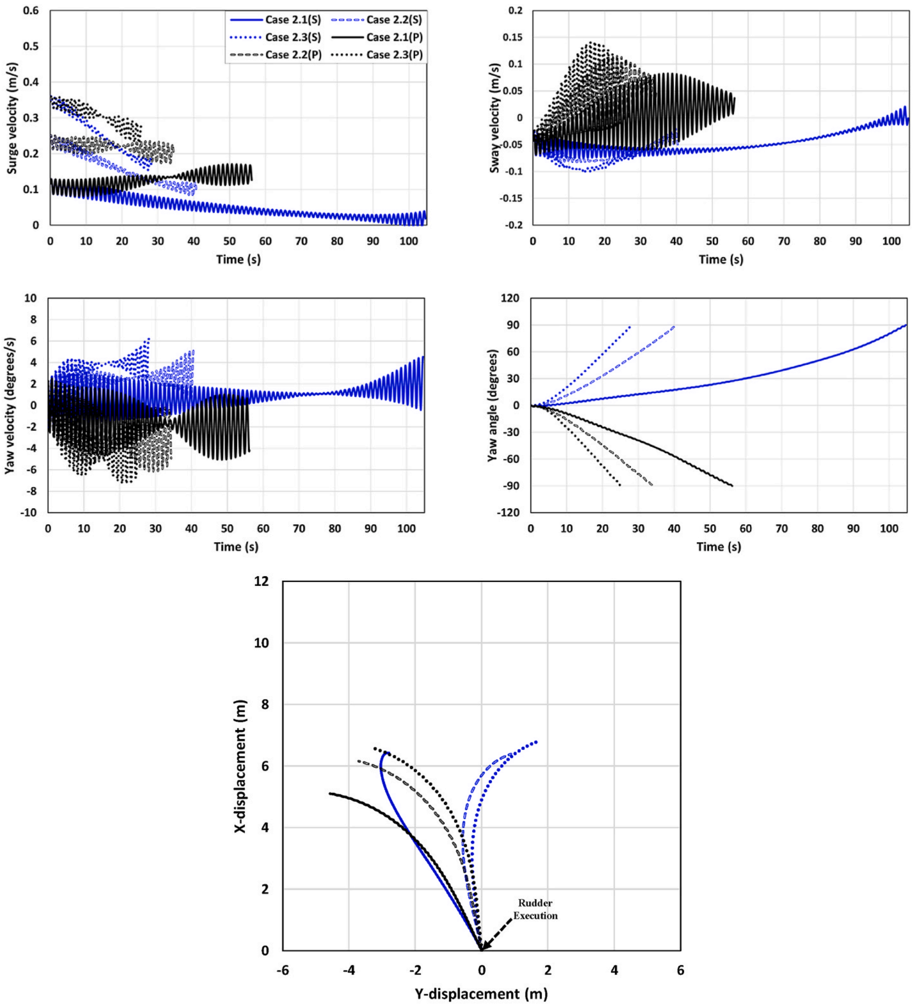

(b) Case 2 (Bow sea)

Fig. 12. (*continued*).

the ship straight. K_p K_i, and K_d indicate the proportional, integral, and derivative control gains, respectively. For the present CFD model, the control gains were determined by the trial-and-error method ($K_p = 5$, $K_i = 0.05$, *and* $K_d = 3$). As presented in Fig. 7, the target yaw angle is determined from the course-keeping module and the PID controller computes the necessary rudder deflection angle with the consideration of the difference between the instantaneous yaw angle and target yaw angle to enable the ship to sail straight. The control module for the free-running manoeuvre was implemented using the report and field function within the CFD software package.

Regarding the turning capability of the ship, the standard turning manoeuvres were performed based on the control functions given in Eqs. (8) and (9):

$$\delta(t) = \begin{cases} \min(0, -kt), & -35 < \delta \leq 0 \\ -35 \end{cases} \text{(Starboard turn)} \tag{8}$$

$$\delta(t) = \begin{cases} \max(0, kt), & 0 \leq \delta < 35 \\ 35 \end{cases} \text{(Port turn)} \tag{9}$$

in which k stands for the maximum rudder rotational rate. The maximum rudder rate is set to $k = 20.1°/\text{s}$ corresponding to $2.32°/\text{s}$ on full scale according to the experimental data.

2.3. Step 3: Free running simulations

The free-running manoeuvres prescribed in Step 1 were carried out to investigate the manoeuvrability of the KCS model with low advance speeds in adverse weather conditions, using the CFD model developed in line with the numerical schemes provided in Step 2.

3. Results

3.1. Verification and validation study

In these authors' previous work (Kim et al., 2021c), the numerical uncertainties of the free-running CFD model using the same numerical methodology have been quantified by carrying out a grid and time-step sensitivity study. As presented in Kim et al. (2021c), CFD uncertainties for critical turning parameters (obtained from the free-running simulations for the KCS in head waves) were estimated to be a maximum of 0.28% in the spatial convergence study and 0.19% in the temporal convergence study by means of Grid Convergence Index (GCI) method.

Additionally, in Kim et al. (2021c)'s study, the trajectory and the time histories of kinematic parameters and ship motions were reported and compared with those measured from the free-running tests by Hiroshima University (Yasukawa et al., 2021). As an example, some of the comparison results reported in Kim et al. (2021c) are presented in Fig. 8. In their work, the approach speed was 0.86 m/s (14.5 knots at full scale)

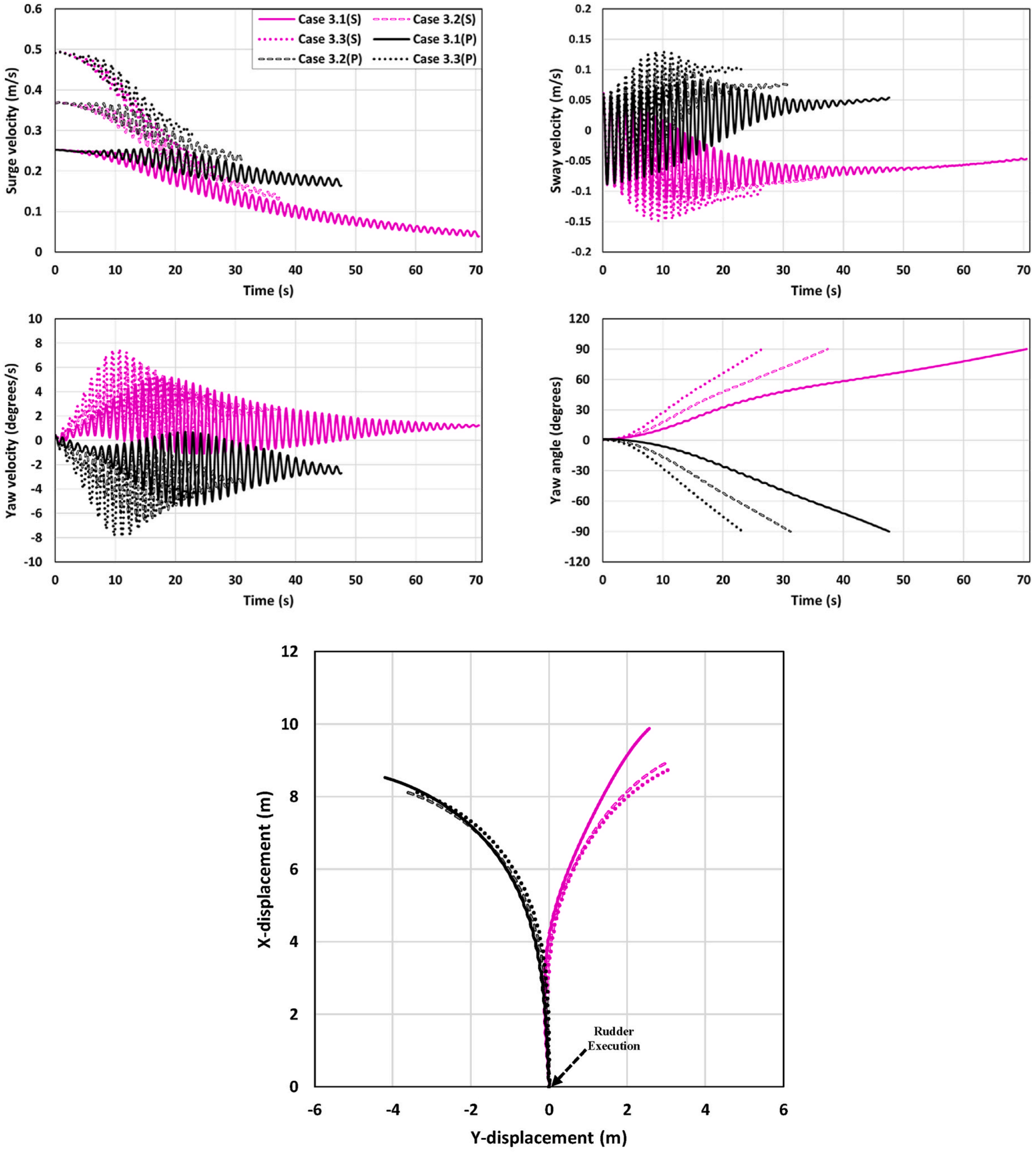

(c) Case 3 (Beam sea)

Fig. 12. (*continued*).

in both calm water (Fig. 8 (a)) and head waves (Fig. 8 (b)). The propeller rotation rate (a: 10.56 RPS, b: 13.38 RPS) was frozen after the ship achieved the self-propulsion condition. Then, the rudder blade was deflected to a maximum of 35° for the turning circle manoeuvre. It can be seen that the agreement between the CFD predictions and the results provided by the experiment is fairly reasonable, demonstrating the capabilities of the current CFD model in predicting manoeuvring problems in waves. Taking this into consideration, it can be claimed that the CFD model adopted in this study is sufficiently validated and reliable for assessing the ship manoeuvrability in question.

3.2. Course keeping control

As stated previously, the self-propulsion computation for each case was first performed to reach the target approach speed. The course keeping manoeuvres were then carried out based on the PID controller designed for changing the rudder deflection angle according to the target yaw angle specified in the manoeuvre, allowing the ship to move in full 6 DOF after the self-propulsion condition was attained. It has to be mentioned that the computations for the course-keeping manoeuvre were run for 8s of model scale time, corresponding to approximately 70s of full-scale time.

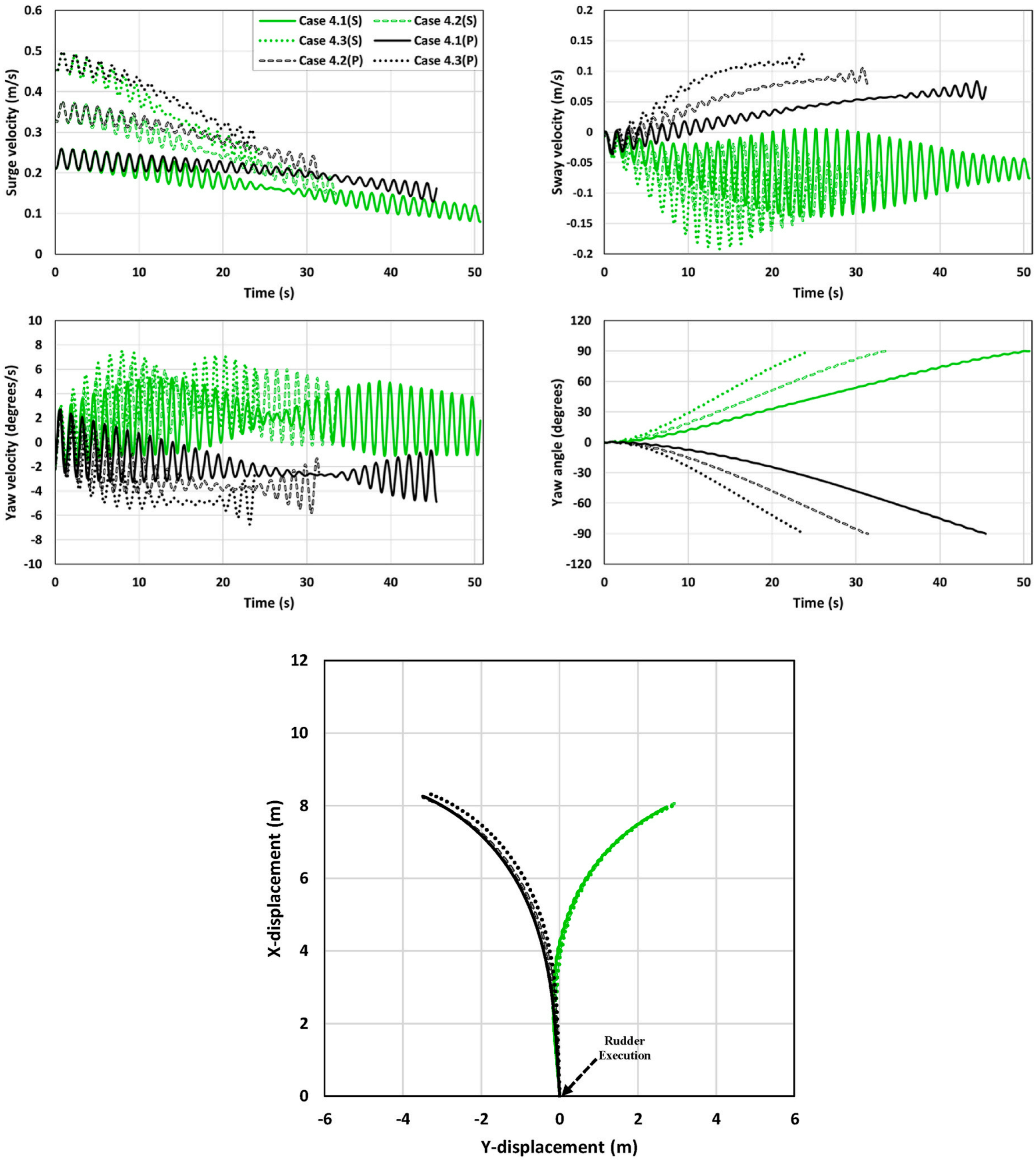

(d) Case 4 (Quartering sea)

Fig. 12. (*continued*).

3.2.1. Ship speed, ship motions, forces, and moments

Fig. 9 shows the time histories of the approach speed, ship resistance, pitch motion, and heave motion experienced by the ship performing the turning manoeuvre for all the cases. Fourier Series (FS) analysis was utilised to process and analyse the unsteady time histories of the force and motions characterised by periodic oscillations due to incident waves. A continuous periodic time series $\varphi(t)$ can be represented with only cosine transforms as given by:

$$\varphi(t) = \varphi_0 + \sum_{n=1}^{\infty} \varphi_n \cdot \cos(2\pi f_e n t + \gamma_n),\ \ n = 1, 2, 3, \ldots \tag{10}$$

$$\varphi_0 = \frac{1}{T}\int_0^T \varphi(t)dt \tag{11}$$

$$\varphi_n = \sqrt{{a_n}^2 + {b_n}^2} \tag{12}$$

$$\gamma_n = \arctan\left(\frac{b_n}{a_n}\right) \tag{13}$$

$$a_n = \frac{2}{T}\int_0^T \varphi(t)\cdot\cos(2\pi f_e n t)dt \tag{14}$$

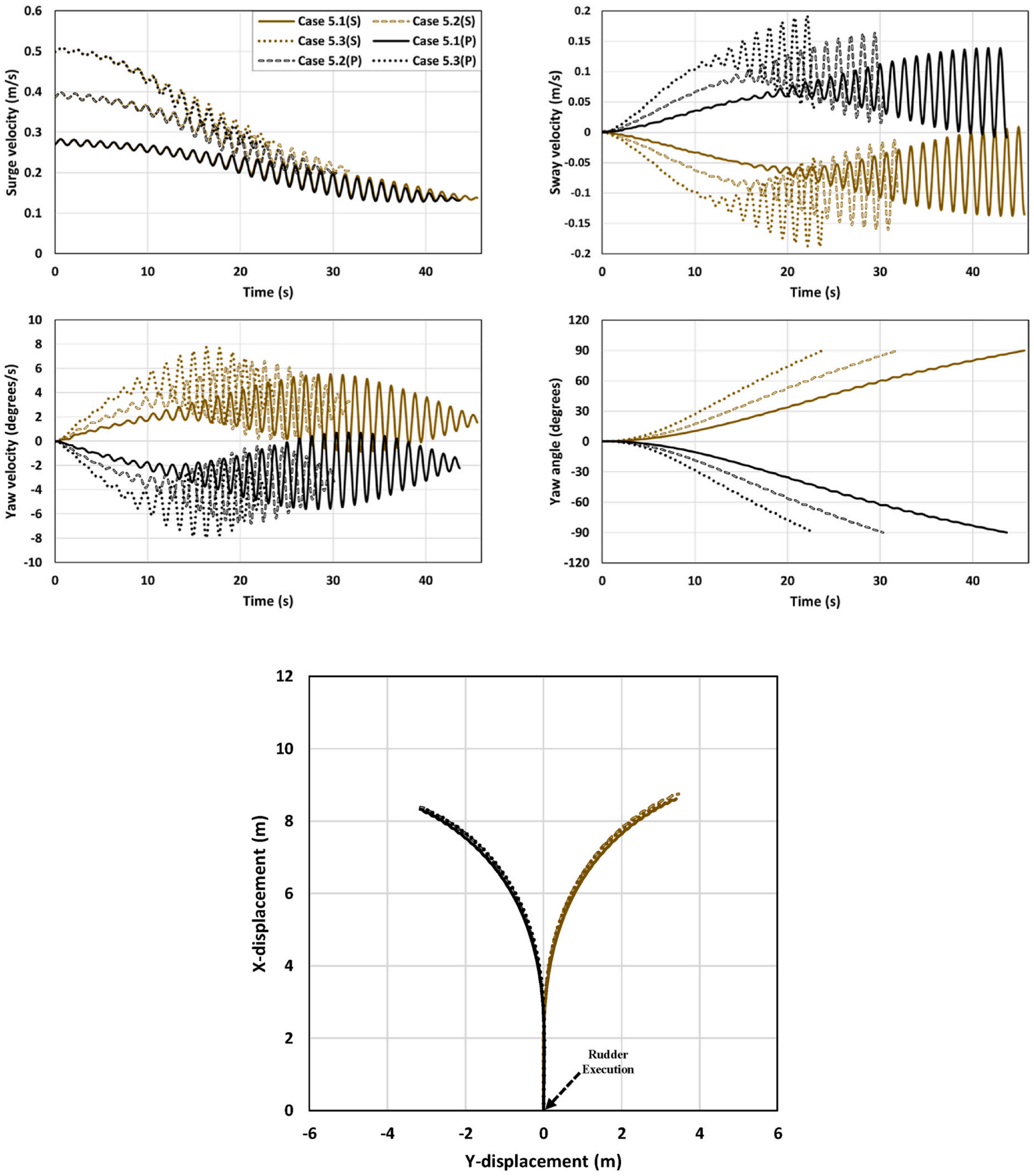

(e) Case 5 (Following sea)

Fig. 12. (*continued*).

$$b_n = -\frac{2}{T}\int_0^T \varphi(t)\cdot sin(2\pi f_e nt)dt \tag{15}$$

where φ_n and γ_n indicate the n th harmonic amplitude and the corresponding phase, respectively. f_e is the encounter frequency of waves and T denotes the total period of the time series for the simulation of the course-keeping manoeuvre. In this study, the zeroth and first harmonic FS terms (regarded as the fundamental components in the linear system) for the force and motions were calculated, as reported in Table 3. The mean value of the time history of the CFD results is represented by the 0th FS harmonic (φ_0), while the average amplitude of the oscillation is represented by the 1st FS harmonic (φ_1).

The results reported in Fig. 9 and Table 3 jointly suggest that the ship performance during the course-keeping manoeuvre showed a remarkable variation depending on the propulsion power and the wave propagation direction. It should be reminded that the three model propulsion points (3.37, 4,87, and 6.35 RPS) corresponding to the full-scale speeds of 2.0, 4.0, and 6.0 knots in head waves were applied throughout all the manoeuvring simulations. As for the approach speed depicted in Fig. 9 (a), an increase in the propulsion power led to the increase of the approach speed for each case, as expected. It is interesting to note that the relatively smaller approach speed was observed in Cases 1 and 2 when compared to the other cases under the condition of the same

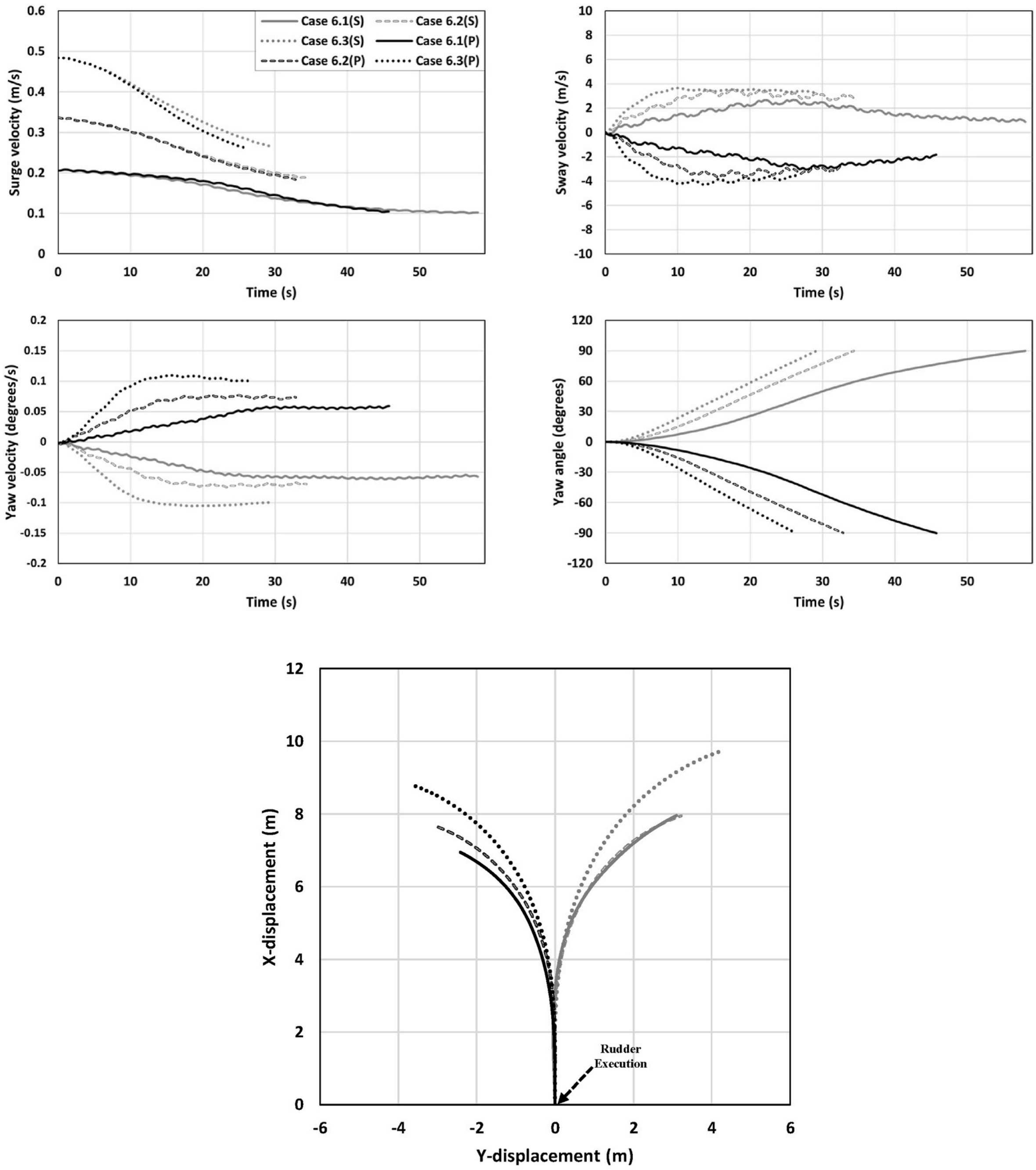

(f) Case 6 (Calm sea)

Fig. 12. (*continued*).

propeller revolution. This was mainly attributed to the differences in the ship resistance and the propeller performance varying depending on the incident wave direction. In addition, it was observed that the ship experienced different oscillation amplitudes for the approach speed depending on the propeller revolution and the wave propagation direction, which is closely associated with the ship motions induced by the waves. For each case (e.g., Cases 1.1, 1.2, and 1.3), the ship resistance was observed to be proportional to the approach speed affected by the propulsion power applied to the ship, clearly evidenced in Fig. 9 (b). It was also seen that the wave propagation direction resulted in the different increase of the resistance as the propeller revolution increased, due to the difference in the added wave resistance experienced by the ship. The ship resistance predicted in the bow and quartering waves showed relatively large oscillation amplitudes regardless of the propulsion power, whilst only very small oscillation amplitudes were observed in the beam and calm sea conditions; this was mainly related to the pitch amplitude experienced by the ship performing the course-keeping manoeuvre. As seen in Fig. 9 (c), the differences in the amplitude of the pitch motions in waves were remarkable according to the incident wave conditions, showing the similar trend of the resistance amplitude.

It was found that the ship experienced a relatively large pitch motion when performing the low-speed course-keeping manoeuvre in the oblique waves (i.e., the bow and quartering waves), as confirmed in Fig. 9 (c) and Table 3. The mean amplitudes of the pitch motion for the bow wave conditions, i.e., Cases 2.1, 2.2, and 2.3, were predicted at 1.13°,

Table 4
CFD results: critical turning indices for all cases.

Parameters (CFD results)	Case 1 (Head sea)					
	Case 1.1(S)	Case 1.2(S)	Case 1.3(S)	Case 1.1(P)	Case 1.2(P)	Case 1.3(P)
Advance (m)	3.55 (1.16L_{BP})	5.38 (1.76L_{BP})	6.29 (2.06L_{BP})	3.49 (1.14L_{BP})	5.23 (1.71L_{BP})	6.13 (2.00L_{BP})
Transfer (m)	1.96 (0.64L_{BP})	2.38 (0.77L_{BP})	2.59 (0.84L_{BP})	1.79 (0.58L_{BP})	2.19 (0.71L_{BP})	2.39 (0.78L_{BP})
Time for yaw 90 degrees (s)	50.59	34.07	25.61	47.94	32.45	24.58
	Case 2 (Bow sea)					
	Case 2.1(S)	Case 2.2(S)	Case 2.3(S)	Case 2.1(P)	Case 2.2(P)	Case 2.3(P)
Advance (m)	6.41 (2.09L_{BP})	6.38 (2.08L_{BP})	6.78 (2.21L_{BP})	5.09 (1.66L_{BP})	6.15 (2.01L_{BP})	6.60 (2.16L_{BP})
Transfer (m)	2.79 (0.91L_{BP})	0.88 (0.28L_{BP})	1.68 (0.55L_{BP})	4.57 (1.49L_{BP})	3.70 (1.21L_{BP})	3.34 (1.09L_{BP})
Time for yaw 90 degrees (s)	104.59	40.65	28.11	56.19	34.35	25.28
	Case 3 (Beam sea)					
	Case 3.1(S)	Case 3.2(S)	Case 3.3(S)	Case 3.1(P)	Case 3.2(P)	Case 3.3(P)
Advance (m)	9.88 (3.23L_{BP})	8.95 (2.92L_{BP})	8.76 (2.86L_{BP})	8.52 (2.78L_{BP})	8.14 (2.66L_{BP})	8.13 (2.65L_{BP})
Transfer (m)	2.56 (0.83L_{BP})	3.04 (0.99L_{BP})	3.11 (1.01L_{BP})	4.19 (1.37L_{BP})	3.69 (1.20L_{BP})	3.41 (1.11L_{BP})
Time for yaw 90 degrees (s)	70.47	37.41	26.46	47.60	31.20	23.23
	Case 4 (Quartering sea)					
	Case 4.1(S)	Case 4.2(S)	Case 4.3(S)	Case 4.1(P)	Case 4.2(P)	Case 4.3(P)
Advance (m)	7.94 (2.59L_{BP})	8.05 (2.63L_{BP})	8.00 (2.61L_{BP})	8.26 (2.70L_{BP})	8.22 (2.69L_{BP})	8.34 (2.72L_{BP})
Transfer (m)	2.69 (0.88L_{BP})	2.92 (0.95L_{BP})	2.93 (0.96L_{BP})	3.49 (1.14L_{BP})	3.48 (1.13L_{BP})	3.36 (1.09L_{BP})
Time for yaw 90 degrees (s)	50.66	33.48	24.35	45.45	31.42	23.79
	Case 5 (Following sea)					
	Case 5.1(S)	Case 5.2(S)	Case 5.3(S)	Case 5.1(P)	Case 5.2(P)	Case 5.3(P)
Advance (m)	8.61 (2.81L_{BP})	8.74 (2.86L_{BP})	8.61 (2.81L_{BP})	8.32 (2.72L_{BP})	8.37 (2.73L_{BP})	8.31 (2.71L_{BP})
Transfer (m)	3.39 (1.10L_{BP})	3.46 (1.13L_{BP})	3.31 (1.08L_{BP})	3.16 (1.03L_{BP})	3.15 (1.03L_{BP})	3.04 (0.99L_{BP})
Time for yaw 90 degrees (s)	45.55	31.86	23.79	43.65	30.31	22.86
	Case 6 (Calm sea)					
	Case 6.1(S)	Case 6.2(S)	Case 6.3(S)	Case 6.1(P)	Case 6.2(P)	Case 6.3(P)
Advance (m)	7.95 (2.60L_{BP})	7.94 (2.59L_{BP})	9.71 (3.17L_{BP})	6.94 (2.27L_{BP})	7.68 (2.51L_{BP})	8.79 (2.87L_{BP})
Transfer (m)	3.10 (1.01L_{BP})	3.21 (1.05L_{BP})	4.19 (1.37L_{BP})	2.41 (0.79L_{BP})	3.09 (1.01L_{BP})	3.64 (1.19L_{BP})
Time for yaw 90 degrees (s)	58.04	34.33	29.29	45.75	32.85	26.28

1.27°, and 1.29°, respectively, whilst the mean pitch amplitudes for the quartering wave conditions, i.e., Cases 4.1, 4.2, and 4.3, were observed at 1.02°, 0.95°, and 0.91°, respectively. It was noted that the pitch amplitudes in the other cases were remarkably smaller than those in Cases 2 and 4. For the sake of clear comparison, the pitch responses are non-dimensionalised by wave steepness (H/λ) in Table 3. It is noteworthy to mention that the pitch motion was observed to vary depending on the propulsion power (i.e., the approach speed) under the condition of the same incident wave direction, which was intimately correlated with the encounter frequency of the incident wave. For example, the amplitude of the pitch motion in Case 2 became progressively larger as the propeller revolution (i.e., the approach speed) increased. It resulted from the fact that the frequency of encounter of the waves (f_e) became close to the natural frequency of the heaving and pitching motions (f_n) with an increase in the propulsion power; the encounter frequencies for Cases 2.1, 2.2, and 2.3 are 0.849, 0.886, and 0.920 Hz, respectively. It has to be stated that for the KCS model considered in this work, the natural frequencies of the heaving and pitching system were observed close to $f_n \approx 0.93$ Hz, as presented in Kim et al. (2021c). On the other hand, the opposite trend was observed for

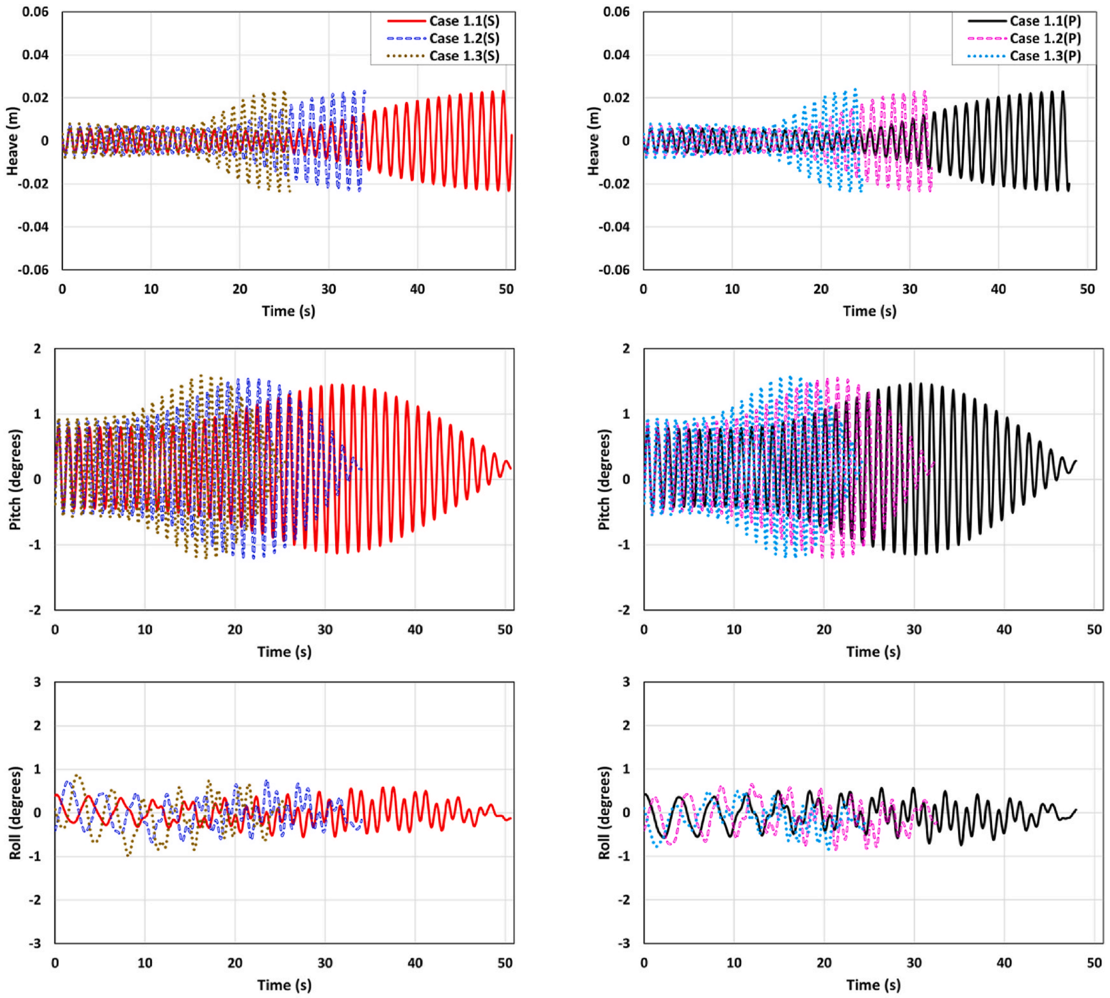

(a) Case 1 (Head sea)

Fig. 13. The time histories of the heave and pitch motions experienced by the ship performing the turning manoeuvre; left column: starboard turns and right column: port turns.

Case 4 as the propeller revolution increased. The pitch amplitude in Case 4 decreased with an increase in the propulsive power, which can be explained by the fact that the encounter frequency in the quartering waves became far away from the natural frequency as the approach speed increased; the encounter frequencies for Cases 4.1, 4.2, and 4.3 are 0.745, 0.710, and 0.672 Hz, respectively. As seen in Fig. 9 (d) and Table 3, the trend observed for the heave motion in waves was largely similar to the behaviour of the pitch motion, apart from Case 3 (the beam wave conditions). It clearly appeared that the ship operating in the beam waves experienced the maximum vertical motion almost equal to the incident wave amplitude, regardless of the propulsion power. This can be explained by the fact that the heave motion has a correlation with the ratio of wavelength to ship length. The ship breadth can be assumed to be the relevant length when the ship was moving forward in the beam waves, which is relatively smaller than the wavelength (the breadth is about 82% smaller than the wavelength in this work). Such a small relevant length may result in the maximum heave excitation force on the ship, thus the maximum heave motion. The heave responses are also non-dimensionalised by wave amplitude (H/2) in Table 3. The pitch and heave motions in calm water (i.e., Case 6) were found to be negligible as only very small amplitudes during the course-keeping manoeuvre were observed because of the absence of external disturbances.

3.2.2. *Course keeping capabilities*

In the course-keeping manoeuvre, the ship was advancing forward at a constant propeller rotational speed in the given environment, deflecting the rudder blade according to the PID controller to attain the target yaw angle (which was set at 0° in this study). In order to compare the course-keeping capability for the different propulsive powers, the time histories of the ship's heading angle and rudder deflection angle under the course-keeping manoeuvres are reported in Fig. 10. It can be observed that the heading control to achieve the target yaw angle was successfully implemented based on the prescribed control mechanism throughout all the cases even including the lowest model propulsion point (3.37 RPS) corresponding to full-scale 2 knots in head waves. This could imply that the guidelines for the minimum required advance speed to maintain a ship's manoeuvrability, which was put forward by the MEPC (IMO, 2021), is considered satisfactory for the KCS model performing the course-keeping manoeuvre in adverse weather conditions. It has to be stated that a similar analysis was carried out in Kim et al. (2022d), the manoeuvrability of the KVLCC2 in adverse weather conditions was investigated in consideration of the minimum propulsion power to maintain a ship's manoeuvrability. Their investigation demonstrated that the KVLCC2 model performing the course-keeping manoeuvre with low advance speeds cannot attain the desired headings when operating in port beam and port stern quartering waves (even the rudder was deflected to a maximum of 35° to control the heading

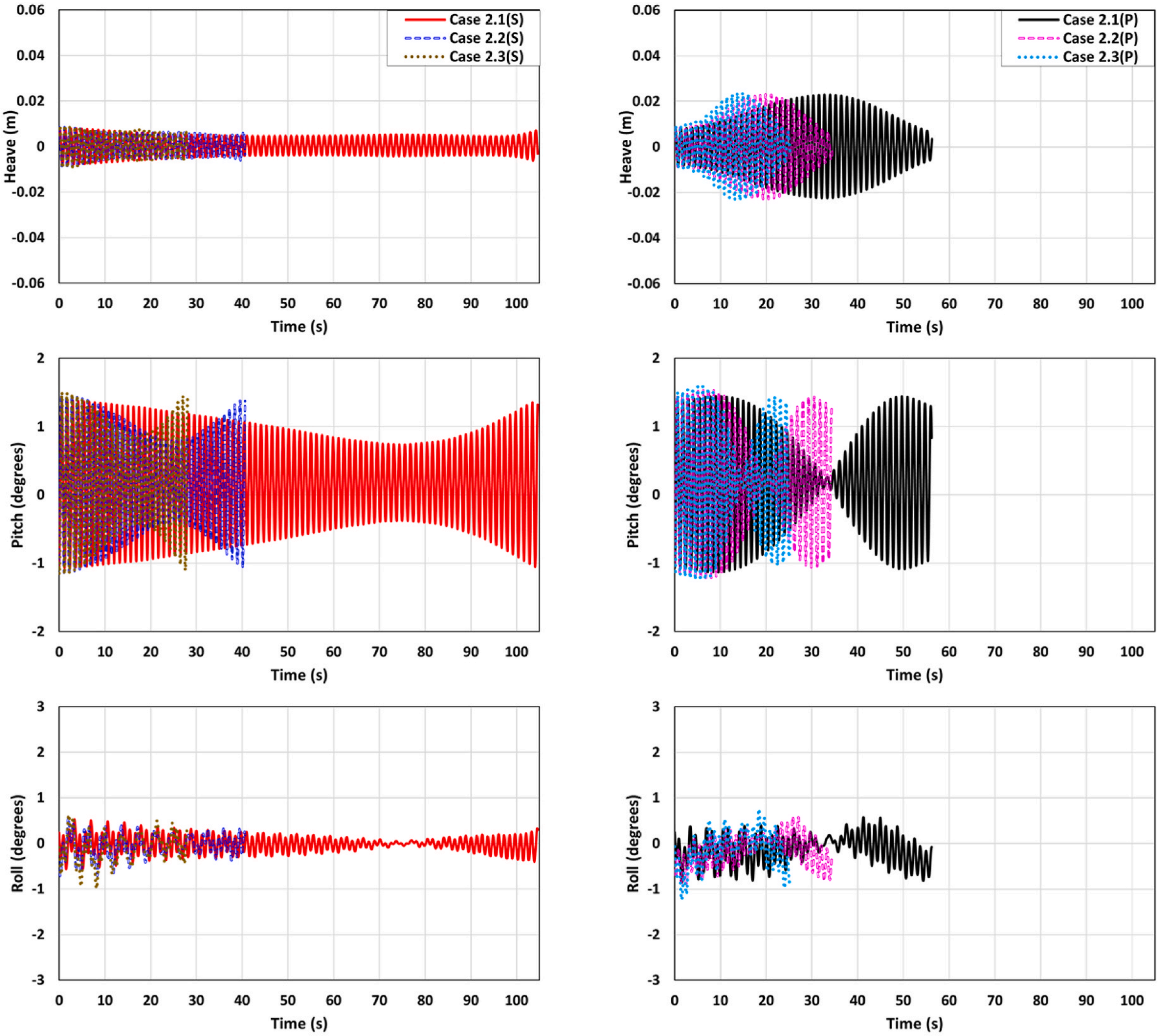

(b) Case 2 (Bow sea)

Fig. 13. (*continued*).

angle). This indicates that the KCS is more manoeuvrable at low speeds than the KVLCC2 due to its slenderness. Given this, the limitation of the guidelines for determining minimum propulsion power to maintain the manoeuvrability in adverse conditions could be found in the fact that the course-keeping capability is different depending on the types and dimensions of subject vessels. It is expected that the greater the block coefficient (C_B) of a ship, the greater the minimum required advance speed can be to ensure sufficient manoeuvrability, as evidenced in the results of the course-keeping manoeuvre for the KCS and KVLCC2.

From Fig. 10, it clearly appeared that only small rudder deflection angles were observed when the ship was performing the course-keeping manoeuvre in the head (Case 1), following (Case 5), and calm (Case 6) seas, regardless of the propeller revolution applied. This means that the ship's heading control was not an issue when performing low-speed course-keeping manoeuvres in the head, following, and calm seas, mainly stemming from the symmetric pressure distribution on both sides of the ship advancing (which does not generate yaw moments and thus yaw deviation). On the other hand, it was observed that the heading control was quite more challenging when advancing in the oblique waves (i.e., Cases 2 and 4), inducing more aggressive steering compared to the other cases. The main reason for larger rudder deflection angles lies in the asymmetric pressure distribution on the hull when carrying out the course-keeping manoeuvre in the oblique waves, resulting in a substantial yaw moment and thus yaw deviation (as discussed in Kim et al. (2021c)). It is important to note that the rudder deflection became larger with a decrease of the propeller revolution for Cases 2 and 4, demonstrating the contribution of the propulsive power to the course-keeping capability. As an example, the maximum rudder deflection for the heading control was predicted to be approximately 16° for Case 2.1 (3.37 RPS), 10° for Case 2.2 (4.87 RPS), and 7° for Case 2.3 (6.35 RPS). In addition, the rudder deflection angle was observed to remain below about 5° when operating in the beam waves (Case 3), showing that the heading control is less challenging than the oblique wave conditions. Given the results presented in Fig. 10, the minimum required advance speed (i.e., 2 knots) adopted by the MEPC could be adequate for a conventional container vessel of similar type and dimensions in terms of the course-keeping manoeuvre in waves.

Fig. 11 displays the predicted trajectories experienced by the ship performing the course-keeping manoeuvre (i.e., the heading control according to the control mechanism). It was identified that a very small deviation from the original course occurred when the ship was moving forward in the head (Case 1), following (Case 5), and calm (Case 6) seas, regardless of the propulsive power applied (mainly due to the symmetric pressure distribution on the ship hull). The ship advancing in the bow seas (Cases 2.1, 2.2, and 2.3) experienced the maximum deviation under the condition of the same propeller revolution, resulting from the asymmetric pressure distribution on the ship causing a substantial lateral force and yaw moment. In a similar manner, it was observed that

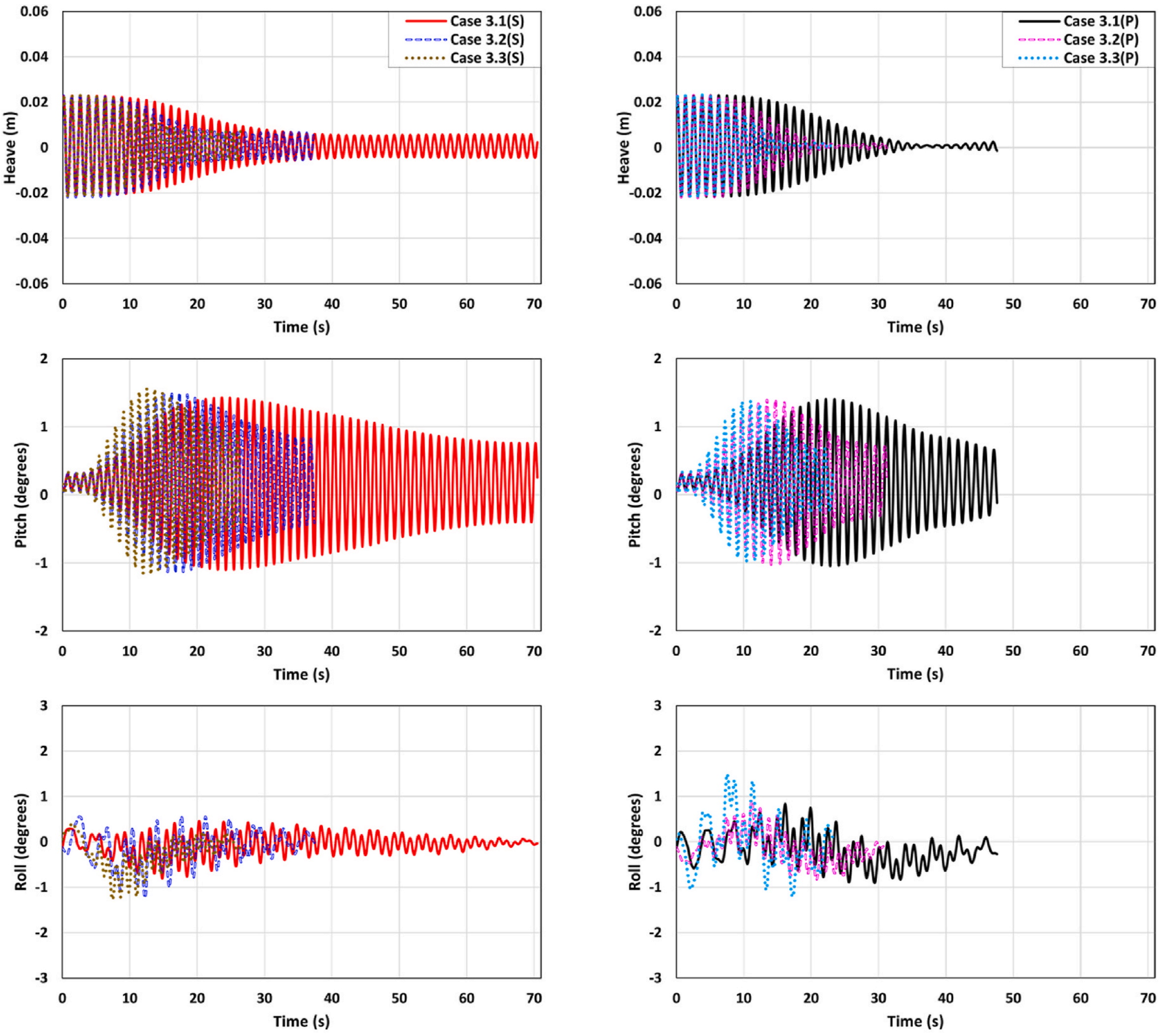

(c) Case 3 (Beam sea)

Fig. 13. (*continued*).

the beam (Case 3) and quartering (Case 4) seas caused a course deviation to some extent. It is worth noting that lower propulsion revolutions (i.e., lower ship advance speeds) can result in a large deviation from the planned route, demonstrating the contribution of insufficient propulsive power to a course deviation. The lower the propulsive power, the larger the difference between the ship's velocity orientation and the ship's heading (i.e., the drift angle) can be when operating in such rough seas (which should be carefully monitored by Master Mariners and navigating officers in practice for safe navigation).

3.3. *Turning circle manoeuvre*

In this sub-section, the results of the free-running simulation for the turning circle manoeuvre will be presented. It should be stated that the turning manoeuvre computation was started from the stable condition of the course-keeping manoeuvre. As shown in Table 2, both the starboard and port turning manoeuvres were carried out in this work, resulting in 36 turning manoeuvre simulation cases (starboard turn: 18 cases and port turn: 18 cases). Throughout all the simulations, the turning circle manoeuvres with only the yaw angle variation of 90° were taken into consideration due to the very long computational time (closely related to the remarkably slow yaw velocity experienced by the ship with the low propulsion power). The computation time for each case was up to 672 wall clock hours with 40 CPU processors.

3.3.1. *Time histories during the turning and turning indices*

Fig. 12 presents the time histories of the ship velocities (i.e., the surge, sway, and yaw velocities), yaw angles, and trajectories during the turning manoeuvre. The ship velocities are referred to the ship-fixed coordinate frame, while the trajectories experienced by the ship are referred to the earth-fixed coordinate frame. In order to quantify the contribution of the propulsion power to the turning performance, the critical turning parameters (i.e., the advance, the transfer, and the time to 90° yaw angle change) were reported in Table 4. ITTC (2021a) can be consulted for detailed information on the important turning indices.

When the ship was turning in the head waves (Cases 1.1–1.3), it was observed that the ship advance and transfer became smaller with a decrease in the propulsive power, as evidenced by the ship trajectories in Fig. 12 (a). In addition, a relatively low propulsion power led to the relatively long time taken for a 90° turn, affecting the rudder normal force which can be decisive for the turning performance. A very similar trend between the starboard and port turns was observed for the ship's velocities in the case of the same propeller revolution (regardless of the sign), consequently resulting in almost symmetric turning trajectories. It is noteworthy to mention that the turning trajectory is directly associated with the ship velocities in the horizontal plane (the surge, sway, and velocities) which can be significantly affected by the propulsive power.

It was revealed that when the ship was advancing in the bow waves

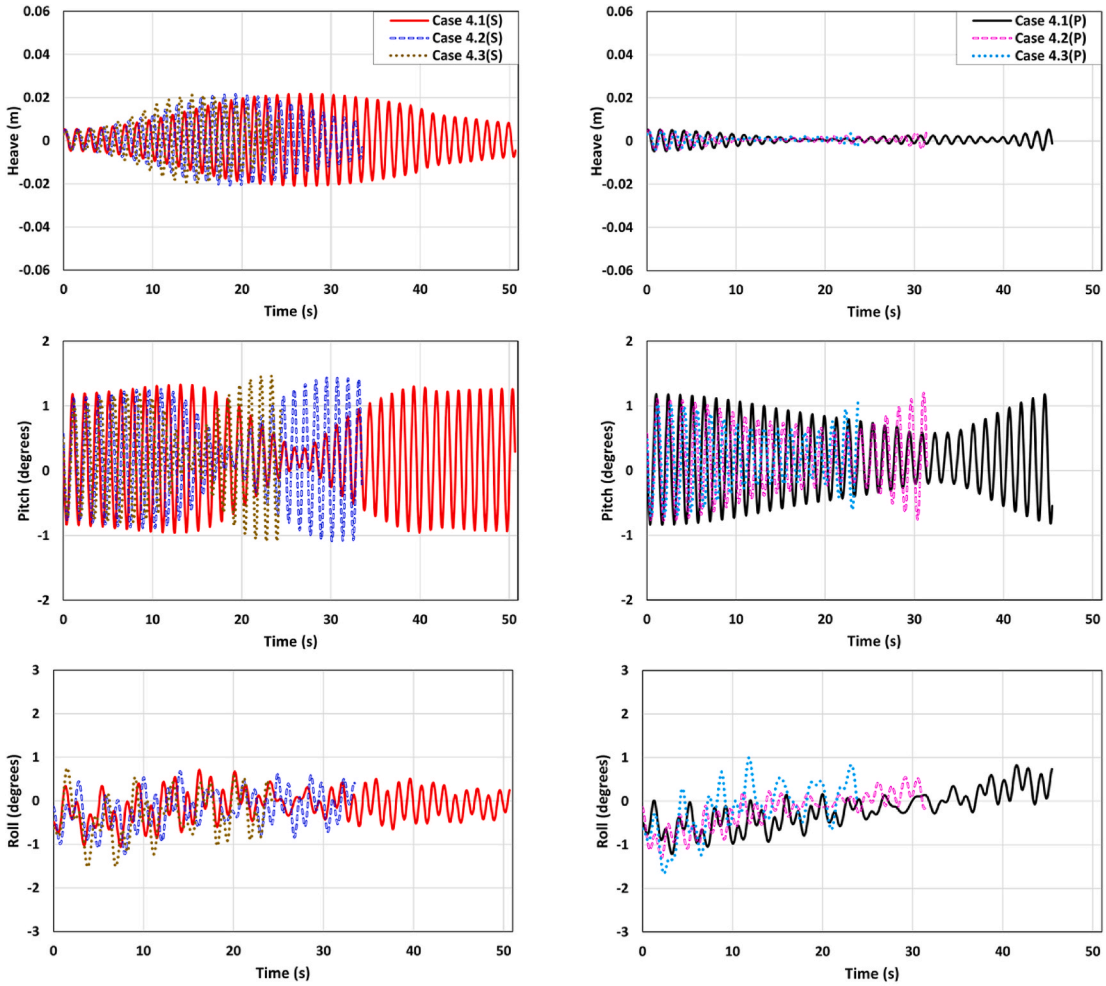

(d) Case 4 (Quartering sea)

Fig. 13. (*continued*).

(Cases 2.1–2.3), the starboard turning manoeuvre is quite challenging, especially for the lowest model propulsion point (Case 2.1, 3.37 RPS). The longest time to turn by 90° (104.59 s) was predicted for the ship performing the starboard turn with the lowest model propulsion point in the bow waves (Case 2.1), having a strong influence on the drift of the ship trajectory. The significant drift of the trajectories (i.e., port-side biased trajectories) was clearly observed for the starboard turns, and the drift direction was consistent with the wave propagation direction. This may imply the lack of sufficient manoeuvrability which may pose a threat to the safe operation of a ship in adverse weather conditions. The port turns in the bow waves were not an issue, on the other hand, demonstrating a relatively short time taken for a 90° turn and successful port turning trajectories. As it can be inferred from Fig. 12 (b), the direction in which the ship was turning is intimately associated with the turning behaviour of the ship operating in waves.

For the turning manoeuvres in the beam waves coming from the starboard side (Cases 3.1–3.3), it was seen that the starboard turning with the lowest model propulsion point (Case 3.1) is relatively challenging, presenting the second-longest time taken for a 90° turn (70.47 s) in this work; the drift of the trajectory was also clearly noted due to the wave drifting forces and moments. As a result, a relatively large advance and a relatively small transfer were observed for the ship performing the starboard turning with the lowest model propulsion point in the starboard beam waves. As can be observed in Fig. 12 (c) and Table 4, the ship advance became progressively larger and the transfer became smaller as the propeller revolution increased in the case of the starboard turns. It should be noted that the direction of the incident wave is opposite to the direction towards which the ship intended to turn at the beginning of the turning manoeuvre. For the port turns, the advance and transfer experienced by the ship decreased with an increase in the propeller revolution. Interestingly, Fig. 12 (d) and (e) highlight the fact that the propulsion power resulted in only a negligible contribution to the turning trajectory when the ship was operating in the quartering and following waves (Cases 4 and 5), contrarily to the other cases. However, it should be noted that the effects of the propulsion power on the ship's velocities during the turning manoeuvre were noticeable. The inherent low-speed turning capability of the ship in calm water (Case 6) can be found in Fig. 12 (f). It was demonstrated that the advance and transfer generally increased with the increase of the propulsive power, attaining a shorter time to turn by 90°. In general, the greater forward speed (due to the larger propulsive power) and the longer time to turn by 90° lead to the larger advance and transfer.

It should be emphasised that the model self-propulsion point was used throughout all the simulations in this work. As a result of the scale effects on ship hydrodynamics, the critical turning indices may differ from those experienced by the full-scale ship.

3.3.2. *Wave-induced motions during turning manoeuvre*

The time histories of the heave, pitch, and roll motions experienced by the ship performing the turning manoeuvre are reported in Fig. 13, in which the left column is for the starboard turns and the right column is for the port turns. It was observed that the heave and pitch motions

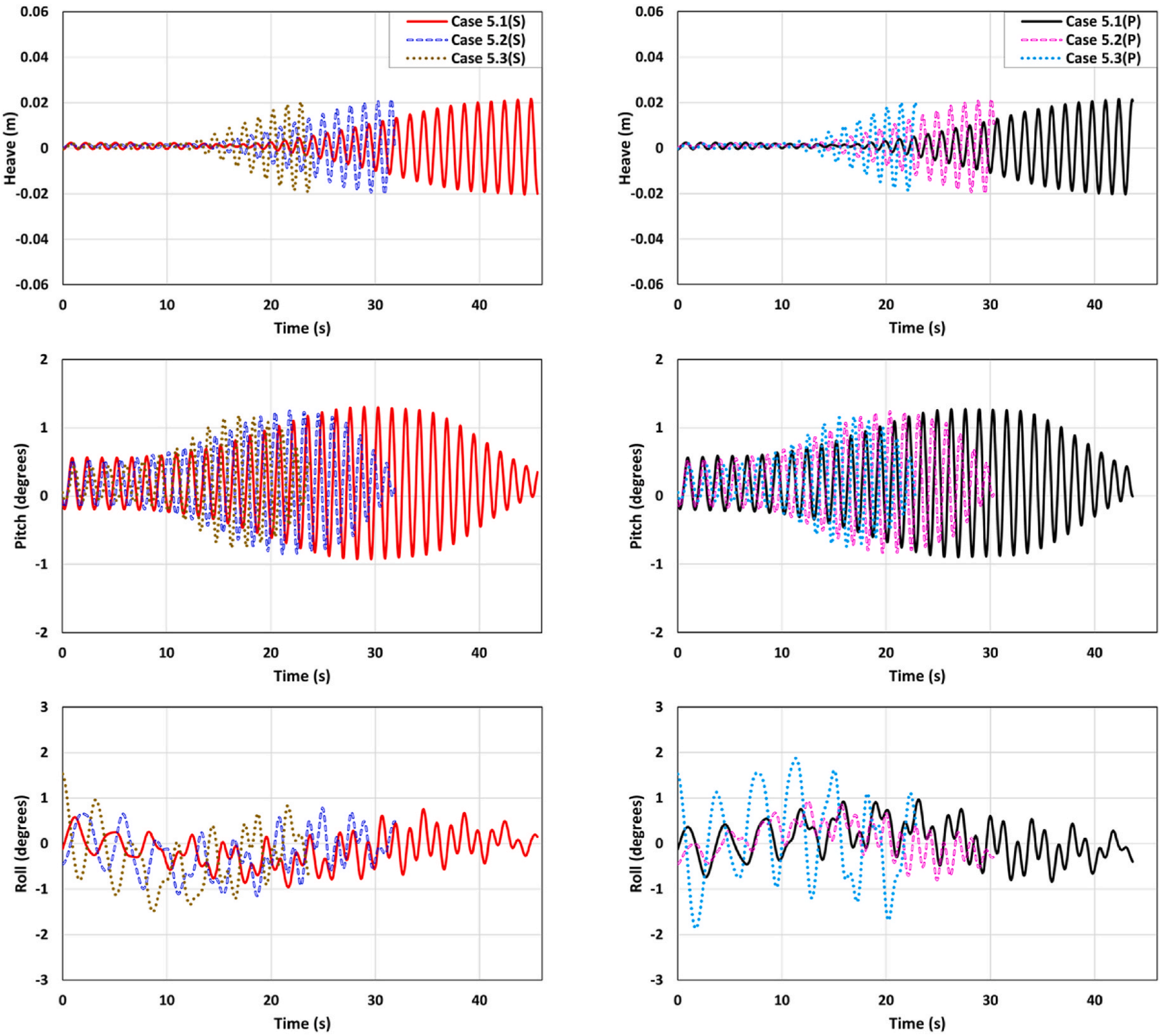

(e) Case 5 (Following sea)

Fig. 13. (*continued*).

changed continuously during the turning manoeuvre, which is closely correlated with the instantaneous changes in the wave-encounter direction. In other words, the heave and pitch excitation forces were significantly affected by the wave-encounter direction during the ship's turning.

The ship advancing in head waves (Case 1) experienced the head wave (0° turn), the bow quartering wave (45° turn), and the beam wave (90° turn) after the start of the turning manoeuvre in a sequential manner. The heave motions were observed to become progressively larger for both the starboard and port turns since the relevant length became longer during the turning manoeuvre. It should be reiterated that the maximum heave excitation force occurs in the beam wave condition, as stated in Section 3.2.1. The amplitude of the pitch motions grew until the ship experienced the bow waves, thereafter it progressively decreased because the beam wave condition caused the minimum pitch motion response. The ship moving forward in the bow waves (Case 2) experienced the starboard bow wave (0° turn), the head wave (45° turn), and the port bow wave (90° turn) in series after the start of the starboard turning manoeuvre. For the port turning manoeuvre, the ship experienced the starboard bow wave (0° turn), the port beam wave (45° turn), the port quartering wave (90° turn) sequentially. As expected, the maximum heave motion and the minimum pitch motion during the ship's turning were noticed in the beam wave condition for Case 2. Similarly, the same analysis can be applied for the rest of the cases. As presented in Kim et al. (2022a), the roll amplitude during the turning manoeuvre has a close correlation with the rudder normal force being affected by the propulsive power. It was observed that only very small roll amplitudes (which remain below 2°) occurred during the turning manoeuvre for all the cases (Cases 1–6), mainly due to the low propulsive power (low-speed manoeuvres).

4. Conclusions and discussion

This study has demonstrated the contribution of low advance speeds to the course-keeping and turning circle manoeuvre in adverse weather conditions, by means of fully nonlinear unsteady RANS simulations. The key findings of this study can be summarised as follows:

For the low-speed course-keeping manoeuvres,

1) It was revealed that the heading control based on the PID controller was not an issue when the ship was performing the low-speed course keeping manoeuvre in the head, beam, following, and calm seas, achieving the desired yaw angle.
2) It was seen that the heading control was quite more challenging when the ship was advancing in the bow and quartering waves. More aggressive steering was observed as the propeller revolution decreased in the oblique waves, indicating the effects of the propulsive power on the course-keeping control.

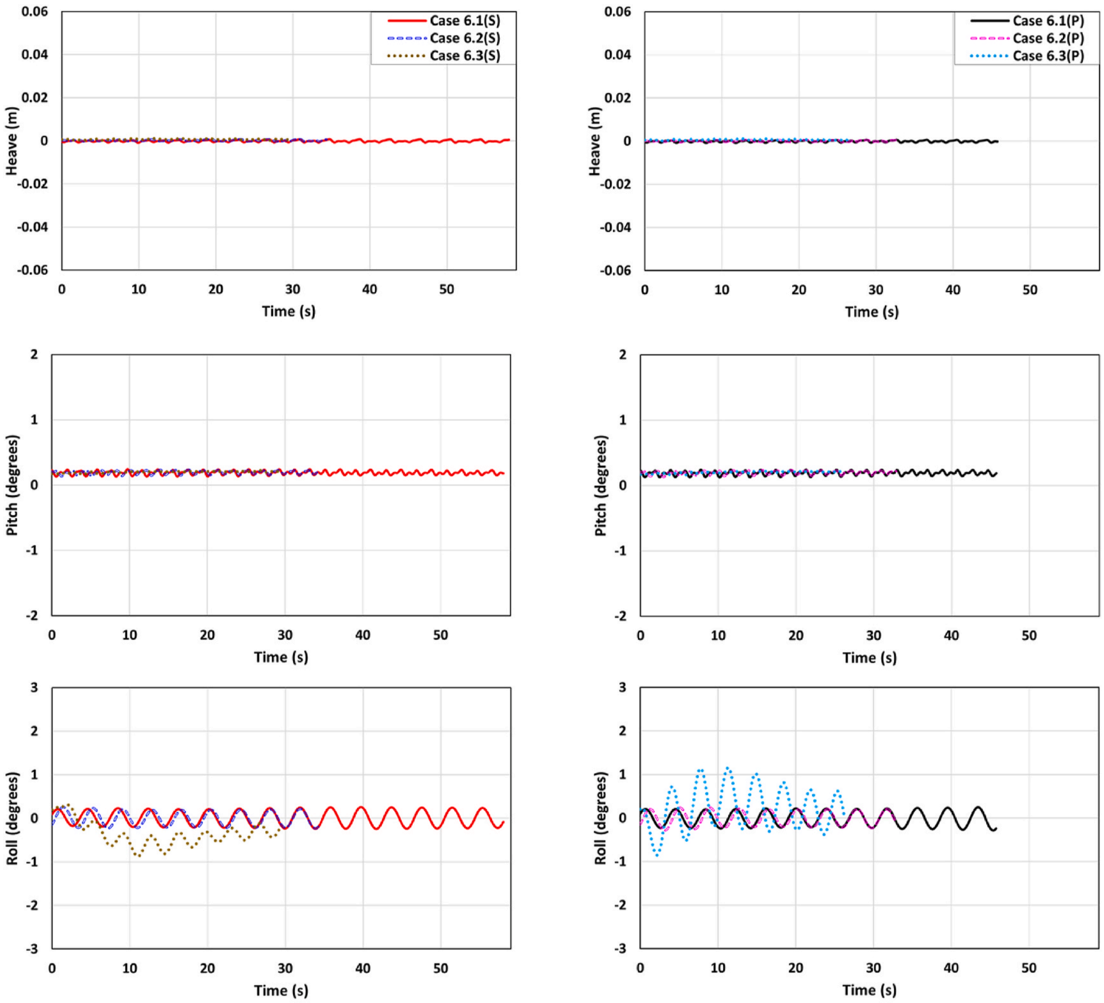

(f) Case 6 (Calm sea)

Fig. 13. (*continued*).

For the low-speed turning circle manoeuvres.

3) The difficulty of the turning manoeuvre was clearly noted when the direction of the incident wave is opposite to the direction towards which the ship intended to turn.
4) Only a negligible effect of the propulsion power on the turning trajectory (starboard turn) was observed when the ship started to turn in the starboard quartering and following waves, compared to the other cases.
5) It appeared that the wave-encounter direction during the ship's turning affected the heave and pitch excitation forces experienced by the ship, thus resulting in a continuous change in the heave and pitch motions.

It can be inferred from the results presented in this work that having minimum propulsion power (based on IMO (2021)) may have a detrimental effect on the safe operation of a ship in rough seas for a certain wave direction. The challenging heading control performance and the significant drift of the trajectories were noted in some cases. It should be borne in mind that the undesired drift of the trajectory can be the main reason for the navigational casualties related to collision, contact and grounding incidents. Based on the results in this study, it is thought that the guidelines regarding the minimum propulsion power should be improved by taking into consideration further important factors such as wave direction. For example, the undesired port-side biased trajectory was observed for the KCS performing the turning manoeuvre with the minimum propulsion power in the bow waves (Case 2.1), indicating that more sufficient propulsion power is needed for safe turning performance. Considering the difference in ship manoeuvrability in adverse weather conditions between the KCS (in this work) and the KVLCC2 (presented in Kim et al. (2022d)), the type of ships should also be an important factor in determining minimum propulsion power.

Recently, maritime autonomous surface ships (MASS) are becoming increasingly attractive as a viable alternative to conventional ships in the commercial maritime sector. The path-following capability of a ship within an acceptable level of safety is a prerequisite for the autonomous ship operation of maritime autonomous systems. Given this, the study can be extended to evaluate the effect of low advance speeds on the path-following capability of a ship in adverse weather conditions by means of a free-running CFD model.

CRediT authorship contribution statement

Daejeong Kim: Writing – original draft, Conceptualization, Methodology, Formal analysis, Investigation, Visualization, Data curation. **Jeongbin Yim:** Conceptualization, Writing – review & editing, Resources. **Soonseok Song:** Methodology, Writing – review & editing, Resources. **Yigit Kemal Demirel:** Methodology, Writing – review & editing, Resources. **Tahsin Tezdogan:** Conceptualization, Methodology, Supervision, Writing – review & editing, Resources.

Declaration of competing interest

The authors declare that they have no known competing financial interests or personal relationships that could have appeared to influence the work reported in this paper.

Data availability

Data will be made available on request.

Acknowledgements

It should be noted that the results were obtained using the ARCHIE-WeSt High Performance Computer (www.archie-west.ac.uk) based at the University of Strathclyde. Part of the present work was also supported by Inha University Research Grant.

References

Broglia, R., Dubbioso, G., Durante, D., Di Mascio, A., 2013. Simulation of turning circle by CFD: analysis of different propeller models and their effect on manoeuvring prediction. Appl. Ocean Res. 39, 1–10.

Broglia, R., Dubbioso, G., Durante, D., Di Mascio, A., 2015. Turning ability analysis of a fully appended twin screw vessel by CFD. Part I: single rudder configuration. Ocean Eng. 105, 275–286.

Carrica, P.M., Mofidi, A., Eloot, K., Delefortrie, G., 2016. Direct simulation and experimental study of zigzag maneuver of KCS in shallow water. Ocean Eng. 112, 117–133.

Choi, J., Yoon, S.B., 2009. Numerical simulations using momentum source wave-maker applied to RANS equation model. Coast. Eng. 56 (10), 1043–1060.

Di Mascio, A., Broglia, R., Muscari, R., 2007. On the application of the single-phase level set method to naval hydrodynamic flows. Comput. Fluid 36 (5), 868–886.

Dubbioso, G., Durante, D., Di Mascio, A., Broglia, R., 2016. Turning ability analysis of a fully appended twin screw vessel by CFD. Part II: single vs. twin rudder configuration. Ocean Eng. 117, 259–271.

el Moctar, O., Sprenger, F., Schellin, T.E., Papanikolaou, A., 2016. Numerical and experimental investigations of ship maneuvers in waves. OMAE2016-54847. In: Proceedings 35th International Conference on Ocean. Offshore and Arctic Engineering, Busan, South Korea, 19-24 June 2016.

Hasanvand, A., Hajivand, A., 2019. Investigating the effect of rudder profile on 6DOF ship turning performance. Appl. Ocean Res. 92, 101918.

Hasanvand, A., Hajivand, A., Ali, N.A., 2021. Investigating the effect of rudder profile on 6DOF ship course-changing performance. Appl. Ocean Res. 117, 102944.

IMO, 2011. AMENDMENTS to the ANNEX of the PROTOCOL of 1997 to AMEND the INTERNATIONAL CONVENTION for the PREVENTION of POLLUTION from SHIPS, 1973, AS MODIFIED by the PROTOCOL of 1978 RELATING THERETO (inclusion of regulations on energy efficiency for ships in MARPOL Annex VI). RESOLUTION MEPC 203 (62).

IMO, 2021. Guidelines for Determining Minimum Propulsion Power to Maintain the Manoeuvrability of Ships in Adverse Conditions.

ITTC, 2011. ITTC - Recommended Procedures and Guidelines : Practical Guidelines for Ship CFD Applications.

ITTC, 2021a. ITTC - Recommended Procedures and Guidelines: Full Scale Manoeuvring Trials.

ITTC, 2021b. The Manoeuvring Committee Final Report and Recommendations to the 29th ITTC.

Kavli, H.P., Oguz, E., Tezdogan, T., 2017. A comparative study on the design of an environmentally friendly RoPax ferry using CFD. Ocean Eng. 137, 22–37.

Kim, D., Song, S., Jeong, B., Tezdogan, T., 2021a. Numerical evaluation of a ship's manoeuvrability and course keeping control under various wave conditions using CFD. Ocean Eng. 237, 109615.

Kim, D., Song, S., Jeong, B., Tezdogan, T., Incecik, A., 2021b. Unsteady RANS CFD simulations of ship manoeuvrability and course keeping control under various wave height conditions. Appl. Ocean Res. 117, 102940.

Kim, D., Song, S., Sant, T., Demirel, Y.K., Tezdogan, T., 2022a. Nonlinear URANS model for evaluating course keeping and turning capabilities of a vessel with propulsion system failure in waves. Int. J. Nav. Archit. Ocean Eng. 14, 100425.

Kim, D., Song, S., Tezdogan, T., 2021c. Free running CFD simulations to investigate ship manoeuvrability in waves. Ocean Eng. 236, 109567.

Kim, D., Tezdogan, T., 2022. CFD-based hydrodynamic analyses of ship course keeping control and turning performance in irregular waves. Ocean Eng. 248, 110808.

Kim, D., Tezdogan, T., Incecik, A., 2022b. A high-fidelity CFD-based model for the prediction of ship manoeuvrability in currents. Ocean Eng. 256, 111492.

Kim, D., Tezdogan, T., Incecik, A., 2022c. Hydrodynamic analysis of ship manoeuvrability in shallow water using high-fidelity URANS computations. Appl. Ocean Res. 123, 103176.

Kim, D.J., Choi, H., Yun, K., Yeo, D.J., Kim, Y.G., 2022d. Experimental study on turning characteristics of KVLCC2 tanker in long-crested irregular waves. Ocean Eng. 244, 110362.

Kim, I.-T., Kim, C., Kim, S.-H., Ko, D., Moon, S.-H., Park, H., Kwon, J., Jin, B., 2021d. Estimation of the manoeuvrability of the KVLCC2 in calm water using free running simulation based on CFD. Int. J. Nav. Archit. Ocean Eng.

Kinaci, O.K., Ozturk, D., 2022. Straight-ahead self-propulsion and turning maneuvers of DTC container ship with direct CFD simulations. Ocean Eng. 244, 110381.

Menter, F.R., 1994. Two-equation eddy-viscosity turbulence models for engineering applications. AIAA J. 32 (8), 1598–1605.

Mofidi, A., Carrica, P.M., 2014. Simulations of zigzag maneuvers for a container ship with direct moving rudder and propeller. Comput. Fluid 96, 191–203.

Muscari, R., Broglia, R., Di Mascio, A., 2008. Trajectory prediction of a self-propelled hull by unsteady RANS computations. In: Proceedings of the 27th ONR Sym- Posium on Naval Hydrodynamics. Korea, Seoul.

Papanikolaou, A., Fournarakis, N., Chroni, D., Liu, S., Plessas, T., Sprenger, F., 2016. Simulation of the maneuvering behavior of ships in adverse weather conditions. In: Proc. 31st Symposium on Naval Hydrodynamics. California, Monterey, pp. 11–16, 11-16 September 2016.

Papanikolaou, A., Zaraphonitis, G., Bitner-Gregersen, E., Shigunov, V., El Moctar, O., Soares, C.G., Reddy, D.N., Sprenger, F., 2015. Energy efficient safe ship operation (SHOPERA). In: Proc. 6th European Transport Research Conference, Transport Research Arena - TRA 2016. Warsaw, 18-21 April, 2016.

Perić, R., Abdel-Maksoud, M., 2018. Analytical prediction of reflection coefficients for wave absorbing layers in flow simulations of regular free-surface waves. Ocean Eng. 147, 132–147.

Shen, Z., Wan, D., Carrica, P.M., 2015. Dynamic overset grids in OpenFOAM with application to KCS self-propulsion and maneuvering. Ocean Eng. 108, 287–306.

Siemens, 2020. Simcenter STAR-CCM+ Documentation.

Song, S., Demirel, Y.K., Muscat-Fenech, C.D.M., Tezdogan, T., Atlar, M., 2020. Fouling effect on the resistance of different ship types. Ocean Eng. 216, 107736.

Sprenger, F., Maron, A., Delefortrie, G., Cura-Hochbaum, A., Papanikolaou, A., 2016. Experimental studies on seakeeping and manoeuvrability in adverse weather conditions. Journal of Ship Research. SNAME Publ.

Terziev, M., Tezdogan, T., Incecik, A., 2020. Application of eddy-viscosity turbulence models to problems in ship hydrodynamics. Ships Offshore Struct. 15 (5), 511–534.

Tezdogan, T., Incecik, A., Turan, O., 2016. Full-scale unsteady RANS simulations of vertical ship motions in shallow water. Ocean Eng. 123, 131–145.

Wang, J., Wan, D., 2018. CFD investigations of ship maneuvering in waves using naoe-FOAM-SJTU Solver. J. Mar. Sci. Appl. 17 (3), 443–458.

Wang, J., Zhao, W., Wan, D., 2016. Self-propulsion simulation of ONR tumblehome using dynamic overset grid method. Shanghai Jiao Tong Univ. Collab. Innovat. Center Adv. Ship Deep-Sea Explor. USA.

Wang, J., Zou, L., Wan, D., 2017. CFD simulations of free running ship under course keeping control. Ocean Eng. 141, 450–464.

Wang, J., Zou, L., Wan, D., 2018. Numerical simulations of zigzag maneuver of free running ship in waves by RANS-Overset grid method. Ocean Eng. 162, 55–79.

Yasukawa, H., Hasnan, M., Matsuda, A., 2021. Validation of 6-DOF motion simulations for ship turning in regular waves. J. Mar. Sci. Technol. 1–16.